Pontifícia Universidade Católica
do Rio de Janeiro

Luis Fernando Cárdenas Castillo

Optical sum rule for quantum geometry in semiconductors

Dissertação de Mestrado

Dissertation presented to the Programa de Pós-graduação em Física of PUC-Rio in partial fulfillment of the requirements for the degree of Mestre em Física.

Advisor: Prof. Wei Chen

Rio de Janeiro
August 2025

Pontifícia Universidade Católica
do Rio de Janeiro

Luis Fernando Cárdenas Castillo

Optical sum rule for quantum geometry in semiconductors

Dissertation presented to the Programa de Pós-graduação em Física of PUC-Rio in partial fulfillment of the requirements for the degree of Mestre em Física. Approved by the Examination Committee:

Prof. Wei Chen
Advisor
Departamento de Física – PUC-Rio

Prof. Tatiana Gabriela Rappoport
CBPF

Prof. Tarik Pereira Cysne
UFF

Rio de Janeiro, August 22nd, 2025

Luis Fernando Cárdenas Castillo

Graduated in Physics from the Universidad Nacional de Ingenieria, Peru, in 2021.

Bibliographic data

Cárdenas Castillo, Luis Fernando

Optical sum rule for quantum geometry in semiconductors / Luis Fernando Cárdenas Castillo; Advisor: Wei Chen. – 2025.

58 f: il. color. ; 30 cm

Dissertação (mestrado) - Pontifícia Universidade Católica do Rio de Janeiro, Department of Física, 2025.

Inclui bibliografia

1. Física – Teses. 2. Absorbância. 3. Função dielétrica. 4. Geometria quântica. 5. Função de Wannier. 6. Semicondutores. 7. Regra da soma óptica. I. Chen, Wei. II. Pontifícia Universidade Católica do Rio de Janeiro. Department of Física. III. Título.

CDD: 530

Acknowledgments

Ao meu orientador Professor Wei Chen pelo estímulo e parceria para a realização deste trabalho.

Ao CNPq e à PUC-Rio, pelos auxílios concedidos, sem os quais este trabalho não poderia ter sido realizado.

Aos meus pais, pela educação, atenção e carinho de todas as horas.

Aos meus colegas da PUC-Rio.

Aos professores que participaram da Comissão examinadora.

A todos os professores e funcionários do Departamento pelos ensinamentos e pela ajuda.

A todos os amigos e familiares que de uma forma ou de outra me estimularam ou me ajudaram.

This study was financed in part by the Coordenação de Aperfeiçoamento de Pessoa de Nível Superior - Brasil (CAPES) - Finance Code 001.

Abstract

Cárdenas Castillo, Luis Fernando; Chen, Wei (Advisor). **Optical sum rule for quantum geometry in semiconductors**. Rio de Janeiro, 2025. 58p. Dissertação de Mestrado – Departamento de Física, Pontifícia Universidade Católica do Rio de Janeiro.

The spatial spread of Wannier functions associated with the valence bands in semiconductors and insulators serves as a fundamental quantity characterizing the degree of electronic localization and, consequently, the insulating behavior of the material. We demonstrate that the gauge-invariant component of this spread can be experimentally accessed through measurements of optical conductivity and absorbance, as both quantities are directly related to the momentum-integrated quantum metric of the valence band states. In three-dimensional systems, integrating the imaginary part of the dielectric function over frequency enables the extraction of the spread of Wannier function. This methodology is illustrated with examples such as silicon (Si), germanium (Ge), and the topological insulator bismuth telluride (Bi_2Te_3). For two-dimensional materials, a similar result is obtained by integrating the absorbance divided by frequency. In the case of graphene, we observe a finite spread arising from intrinsic spin-orbit coupling, which can be probed via absorbance measurement in the microwave range. In twisted bilayer graphene, absorbance in the millimeter-wave regime reveals the presence of nearly flat bands and allows quantification of their associated quantum metric. Finally, we extend our method to hexagonal transition metal dichalcogenides (MX_2, with M = Mo, W and X = S, Se, Te) using a three-band tight-binding model. By translating the formalism into real space, we construct an absorbance marker that permits the study of disorder effects and facilitates comparison with experimental data, thus demonstrating the validity and ubiquity of our approach.

Keywords

Absorbance; Dielectric function; Quantum Geometry; Wannier function; Semiconductors; Optical sum rule.

Resumo

Cárdenas Castillo, Luis Fernando; Chen, Wei. **Regra da soma óptica para geometria quântica em semicondutores**. Rio de Janeiro, 2025. 58p. Dissertação de Mestrado – Departamento de Física, Pontifícia Universidade Católica do Rio de Janeiro.

A extensão espacial das funções de Wannier associadas às bandas de valência em semicondutores e isolantes constitui uma grandeza fundamental para caracterizar o grau de localização eletrônica e, consequentemente, o comportamento isolante do material. Demonstramos que o componente invariante de gauge dessa extensão pode ser determinado experimentalmente por meio de medições da condutividade óptica e da absorbância, uma vez que ambas as quantidades estão diretamente relacionadas à métrica quântica integrada no espaço de momento dos estados da banda de valência. Em sistemas tridimensionais, mostramos que a integração da parte imaginária da função dielétrica em relação à frequência permite extrair diretamente a extensão espacial das funções de Wannier. Essa metodologia é ilustrada com exemplos como o silício (Si), o germânio (Ge) e o isolante topológico telureto de bismuto (Bi_2Te_3). Para materiais bidimensionais, um resultado análogo é obtido integrando a absorbância dividida pela frequência. No caso do grafeno, observamos uma extensão finita decorrente do acoplamento spin-órbita intrínseco, que pode ser investigada por meio de medições de absorbância na faixa de micro-ondas. No grafeno bicamada torcido, a absorbância na faixa de ondas milimétricas revela a presença de bandas quase planas e permite quantificar a métrica quântica associada a elas. Finalmente, estendemos nosso método aos dicalcogenetos de metais de transição com estrutura hexagonal (MX, com M = Mo, W e X = S, Se, Te) utilizando um modelo teórico de bandas reduzidas. Ao traduzir o formalismo para o espaço real, construímos um marcador de absorbância que permite o estudo dos efeitos de impurezas e facilita a comparação com dados experimentais, validando assim a robustez e o poder preditivo da nossa abordagem.

Palavras-chave

Absorbância; Função dielétrica; Geometria quântica; Função de Wannier; Semicondutores; Regra da soma óptica.

Table of contents

List of figures

List of tables

List of Abbreviations

TMD – Transition Metal Dichalcogenide
TBG – Twisted Bilayer Graphene
WS_2 – Tungsten Disulfide
MoS_2 – Molybdenum Disulfide
WSe_2 – Tungsten Diselenide
$MoSe_2$ – Molybdenum Diselenide
WTe_2 – Tungsten Ditelluride
$MoTe_2$ – Molybdenum Ditelluride
BZ – Brillouin Zone
ISOC – Intrinsic Spin-Orbit Coupling
Bi_2Te_3 – Bismuth Telluride
WF – Wannier Function
MLWF – Maximally Localized Wannier Function
QSHE – Quantum Spin Hall Effect

1
Introduction

Recent progress in the study of quantum geometry of Bloch states has notably advanced our comprehension of diverse physical phenomena occurring in solid-state systems. Particularly, quantum geometry naturally emerges in gapped materials such as semiconductors, insulators, and superconductors when considering overlaps between occupied quantum states at neighboring momenta [1]. This gives the Brillouin zone (BZ), interpreted as a compact torus T^D, a structure analogous to a metric tensor. Consequently, various fundamental material properties derived from Bloch states can be expressed in terms of the elements of this quantum metric tensor. For instance, in topological insulators and superconductors, the determinant of the quantum metric directly connects to the absolute value of the curvature function integrated to yield topological invariants [2], placing constraints on the effective volume of the curved BZ [3]. Additionally, due to the intrinsic relationship between quantum metric in semiconductors and insulators and elements of the optical transition matrix, it becomes feasible to extract individual quantum metric components from pump-probe experiments [2] or from data of dielectric functions [4]. This allows further theoretical extensions of quantum metric concepts to interacting systems at finite temperature [5]. Likewise, in conventional superconductors [6], the quantum metric associated with quasihole states considerably affects their optical response, and the metric related to nearly flat bands in the normal state has been linked to the superfluid density observed in superconducting phases [7–12].

This research specifically targets a crucial ground-state characteristic of semiconductors and insulators—the spatial spread of Wannier functions associated with valence bands—which is directly controlled by the quantum metric. This spread is defined by the second cumulant of the electron charge distribution constructed from Wannier functions corresponding to the valence bands. This property has been extensively analyzed through first-principles calculations and Wannierization procedures [13, 14]. The central objective of this thesis is to establish clear and experimentally accessible relationships between the gauge-invariant portion of the spread of Wannier functions, the quantum metric averaged over the Brillouin zone, and the optical matrix

elements appearing in absorption spectra and optical conductivity tensors.

Based on these established relationships, we propose an experimental protocol that enables extracting the gauge-invariant component of the spread of Wannier functions directly from optical conductivity or absorbance measurements. In the case of three-dimensional materials, we show explicitly that the gauge-invariant spread of Wannier functions can be accurately determined by integrating the imaginary component of the dielectric function over frequency, using the known volume of the unit cell and without needing extra fitting parameters. By employing currently available experimental data of dielectric function, we apply this methodology to typical semiconductors such as silicon (Si) and germanium (Ge), as well as to topological insulators like bismuth telluride (Bi_2Te_3) [17–19], thus demonstrating the broad applicability of our approach to a wide variety of 3D semiconductors and insulators.

In two-dimensional systems, we demonstrate that the spread of Wannier functions can be obtained similarly from absorbance data normalized by frequency and subsequently integrated over frequency, again without additional fitting beyond the unit cell area. To illustrate the generality of this method, we select three distinct 2D materials with significantly different characteristic frequency scales. In graphene, we identify a finite spread induced by intrinsic spin-orbit coupling (ISOC), resolving the divergence of the quantum metric at Dirac points [20]. We propose measuring microwave absorbance at sub-Kelvin temperatures to quantify ISOC in graphene. For twisted bilayer graphene (TBG), we utilize a recent tight-binding model to demonstrate how absorbance varies with the twist angle, providing an experimental route to detect the formation of nearly flat bands and quantify the related quantum metric [21]. Finally, employing tight-binding models to hexagonal transition metal dichalcogenides (TMDs), we evaluate their spreads, omitting substrate effects, excitonic interactions, and higher-energy orbitals, and analyzing these systems from both momentum-space and real-space perspectives. To capture additional effects, we consider absorbance data in momentum space and separately develop a real-space absorbance marker based on the fidelity marker concept [24]. Introducing impurities into the samples enables us to compare our theoretical predictions with experimental data to evaluate disorder effects. Specifically, we compare our theoretical results for WS_2 [43, 50, 51] with experimental measurements from samples deposited on fused silica, validating the practical applicability of our experimental procedure.

This thesis is structured as follows: Chapter 2 provides foundational concepts regarding Wannier functions and quantum metric, establishing the theoretical framework, especially highlighting the gauge-invariant part of the spread

of Wannier functions measurable experimentally. Chapter 3 applies these theoretical insights practically, detailing experimental procedures to determine the spreads of Wannier functions in both three-dimensional (semiconductors and topological insulators) and two-dimensional systems (graphene with ISOC, TBG, and TMDs, in the latter including impurity effects). Chapter 4 summarizes the main conclusions drawn from this research and proposes directions for future investigations.

2
Theoretical Background

2.1
Wannier Functions

In a crystal with a periodic lattice, the solutions of the Schrödinger equation take the form:

$$\Psi_{n\boldsymbol{k}}(\boldsymbol{r}) = u_{n\boldsymbol{k}}(\boldsymbol{r})e^{i\boldsymbol{k}\cdot\boldsymbol{r}/\hbar}, \tag{2-1}$$

where $u_{n\boldsymbol{k}}(\boldsymbol{r})$ is a function with the same periodicity as the lattice potential, as a consequence of the Bloch theorem. The vector $\boldsymbol{k}$ is the crystal (quasi)momentum, restricted to the first Brillouin zone (BZ) [15]. The band index n distinguishes different energy bands for each $\boldsymbol{k}$, so these $(n, \boldsymbol{k})$ act like quantum numbers.
This periodicity can be described by the commutativity between the effective Hamiltonian H and the lattice-translation operator $T_{\boldsymbol{R}}$, with $\boldsymbol{R}$ as the Bravais lattice vector, allowing us to choose the common eigenstates according to the prescriptions of the Bloch theorem

$$[\hat{H}, \hat{T}_{\boldsymbol{R}}] = 0, \tag{2-2}$$

i.e $u_{n\boldsymbol{k}}(\boldsymbol{r})$ satisfies the von-Karman periodic boundary conditions [16]

$$u_{n\boldsymbol{k}}(\boldsymbol{r} + \boldsymbol{R}) = u_{n\boldsymbol{k}}(\boldsymbol{r}). \tag{2-3}$$

From eq. (2-1), we see that Bloch functions at different $\boldsymbol{k}$ have different envelope functions $u_{n\boldsymbol{k}}(\boldsymbol{r})$, one can expect to be able to build a localized "wave packet" by superposing Bloch functions of different $\boldsymbol{k}$. To obtain a localized wave packet in the real space, we need to use a very broad superposition in the $\boldsymbol{k}$ space. But $\boldsymbol{k}$ lives in the periodic BZ, so the best we can do is to choose equal amplitudes all across the BZ. Thus, we can construct

$$w_0(\boldsymbol{r}) = \langle \boldsymbol{r}|w_0\rangle = \frac{V_{cell}}{(2\pi\hbar)^3}\int_{BZ} d\boldsymbol{k}\langle \boldsymbol{r}|\Psi_{n\boldsymbol{k}}\rangle, \tag{2-4}$$

where V_{cell} is the primitive cell volume in the real space and the integral is carried over the BZ.

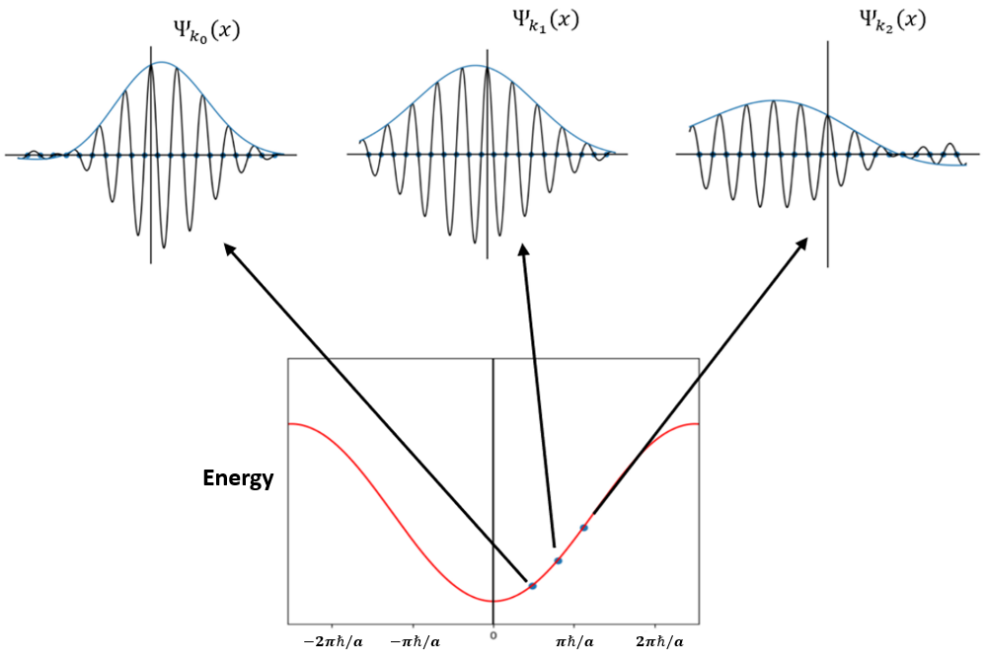

Figure 2.1: Real-space representation of three Bloch functions $e^{ikx}u_k(x)$ associated with a single band in 1D in the first BZ, for three different values of the wave vector k.

Looking at Fig. 2.1, we see a single-band 1D system, where the BZ goes from $-2\pi\hbar/a$ to $2\pi\hbar/a$. Along of the red curve (first band) we see that any value of k gives us an electronic state for the Hamiltonian that is given by a oscillatory part (black curve) times a modulation (blue curve).
In a Dirac notation, we show that $\langle \boldsymbol{r}|n\rangle = e^{-i\boldsymbol{k}\cdot\boldsymbol{r}/\hbar}\langle \boldsymbol{r}|\Psi_{n\boldsymbol{k}}\rangle$, with $\langle \boldsymbol{r}|n\rangle = u_{n\boldsymbol{k}}(\boldsymbol{r})$ and $|n\rangle = |n(\boldsymbol{k})\rangle$, we use the equation (2-4) to define a Wannier state $|\boldsymbol{R}n\rangle$ as

$$\begin{aligned} |n\rangle &= \sum_R e^{-i\boldsymbol{k}\cdot(\boldsymbol{r}-\boldsymbol{R})/\hbar}|\boldsymbol{R}n\rangle \\ |\boldsymbol{R}n\rangle &= \sum_k e^{i\boldsymbol{k}\cdot(\boldsymbol{r}-\boldsymbol{R})/\hbar}|n\rangle, \end{aligned} \tag{2-5}$$

while $\langle \boldsymbol{r}|\boldsymbol{R}n\rangle = W_n(\boldsymbol{r}-\boldsymbol{R})$ stands for the conventional Wannier function (WF) of the charge carrier in the n-th band located around the unit cell at $\boldsymbol{R}$.
If we treat with continuous values of momentum $\boldsymbol{k}$, then we do a integral over the BZ of volume $V_{BZ} = (2\pi)^D/V_{cell}$, i.e

$$\sum_k \longrightarrow \int_{BZ} \frac{d^Dk}{\hbar^D V_{BZ}} = \frac{V_{cell}}{\hbar^D}\int_{BZ}\frac{d^Dk}{(2\pi)^D}, \tag{2-6}$$

then, the Wannier states take the form

$$|\boldsymbol{R}n\rangle = \frac{V_{cell}}{\hbar^D}\int_{BZ}\frac{d^Dk}{(2\pi)^D}|\Psi_{n\boldsymbol{k}}\rangle e^{-i\boldsymbol{k}\cdot\boldsymbol{R}/\hbar}. \tag{2-7}$$

Thus, equation (2-4) can be interpreted as the WF located in the home unit cell.

The equation (2-7) constitutes a unitary transformation between Bloch and Wannier states. Thus, both sets of states provide an equally valid description of the band subspace (since $\{|\boldsymbol{R}n\rangle\}$ span the same space as $\{|\Psi_{n\boldsymbol{k}}\rangle\}$), and even if the WFs are not Hamiltonian eigenstates, unlike Bloch states, still hold orthonormality $\langle \boldsymbol{R}n|\boldsymbol{R}'m\rangle = \delta_{n,m}\delta(\boldsymbol{R}-\boldsymbol{R}')$.

So far, we have carried out a unitary transformation from the Bloch functions to a set of "localized" WFs, such that in a crystal the WFs at different R are translational images of one another, it means that these features are spatially concentrated in a small region around a specific position in the crystal (such as the centers of atoms or bonds), rather than being spread throughout the entire crystal as the Bloch functions.

This means that if we choose a WF centered on a specific cell in the crystal, the function will have significant values only near that cell, and its amplitude will decay rapidly outside that region. In addition, although WFs are spatially localized, they are constructed in such a way that when one considers all WFs for all cells of the crystal, they respect the periodicity of the lattice. In other words, WFs in different cells are related to each other by translations of the crystal lattice

$$W_n(\boldsymbol{r}-\boldsymbol{R}) = W_n(\boldsymbol{r}-(\boldsymbol{R}+\boldsymbol{R}')), \tag{2-8}$$

where $\boldsymbol{R}$ and $\boldsymbol{R}'$ are Bravais lattice vectors on which WFs are centered.

That is, the WFs corresponding to different cells are essentially the same function, but moved to the center of each cell in the network.

2.1.1 Gauge Freedom

As is typical of the wave functions resulting from the Schrödinger equation, these may or may not modify some quantities calculated for the system, depending on the gauge to which they are subjected. Suppose, for instance, we have

$$\begin{aligned} |\tilde{\boldsymbol{R}}n\rangle &= \frac{V_{cell}}{\hbar^D}\int_{BZ}\frac{d^Dk}{(2\pi)^D}\left[e^{i\phi_n(\boldsymbol{k})}|\Psi_{n\boldsymbol{k}}\rangle\right]e^{-i\boldsymbol{k}\cdot\boldsymbol{R}/\hbar} \\ &= \frac{V_{cell}}{\hbar^D}\int_{BZ}\frac{d^Dk}{(2\pi)^D}|\tilde{\Psi}_{n\boldsymbol{k}}\rangle e^{-i\boldsymbol{k}\cdot\boldsymbol{R}/\hbar}, \end{aligned} \tag{2-9}$$

or, equivalently

$$|\tilde{\Psi}_{n\boldsymbol{k}}\rangle = e^{i\phi_n(\boldsymbol{k})}|\Psi_{m\boldsymbol{k}}\rangle. \tag{2-10}$$

The shape of the WFs in real space will be different for each change of phase $\phi_n(\boldsymbol{k})$. Physically, the additional phase does not change the system as

originally described by the Bloch functions; however, it does modify the spatial localization and real-space distribution of the individual WFs.

To describe this spatial distribution, let's define the localization functional

$$\Omega = \sum_n \left[\langle 0n|r^2|0n\rangle - \langle 0n|\boldsymbol{r}|0n\rangle^2 \right] = \sum_n \left[\langle r^2\rangle_n - \bar{\boldsymbol{r}}_n^2 \right]. \tag{2-11}$$

The functional Ω quantifies the total quadratic spread of the WFs associated with the occupied valence bands in the home unit cell (see eq. 2-7). In this expression, the sum over n is performed only over the occupied (valence) bands, so that Ω represents a true ground-state property. This definition ensures that the spread under consideration is physically meaningful and corresponds to an optical sum rule, as we discuss below.

One way to describe this functional, is to decompose it into gauge-dependent and gauge-invariant parts. That is, we can write

$$\Omega = \Omega_I + \tilde{\Omega}, \tag{2-12}$$

where

$$\begin{aligned} \Omega_I &= \sum_n \left[\langle 0n|r^2|0n\rangle - \sum_{Rm} |\langle Rm|\boldsymbol{r}|0n\rangle|^2 \right] \\ \tilde{\Omega} &= \sum_n \sum_{Rm\neq 0n} |\langle Rm|\boldsymbol{r}|0n\rangle|^2. \end{aligned} \tag{2-13}$$

It can be shown that not only $\tilde{\Omega}$ but also Ω_I is positive definite, and moreover that Ω_I is gauge invariant, i.e. invariant under any arbitrary unitary transformation of the Bloch orbitals. The gauge-dependence of $\tilde{\Omega}$ becomes explicit when we use a discretized matrix representation [14].

The next step is to express Ω in terms of Bloch functions. Using the Blount identities [15]:

$$\langle \boldsymbol{R}m|r^l|0n\rangle = \frac{V_{cell}}{\hbar^D}\int_{BZ}\frac{d^Dk}{(2\pi)^D}e^{i\boldsymbol{k}\cdot\boldsymbol{R}/\hbar}\langle m|(i\frac{\partial}{\partial k})^l|n\rangle, \tag{2-14}$$

we can get the expressions

$$\langle \boldsymbol{R}m|r|0n\rangle = i\frac{V_{cell}}{\hbar^D}\int_{BZ}\frac{d^Dk}{(2\pi)^D}e^{i\boldsymbol{k}\cdot\boldsymbol{R}/\hbar}\langle m|\nabla_{\boldsymbol{k}}|n\rangle \tag{2-15}$$

$$\langle \boldsymbol{R}m|r^2|0n\rangle = -\frac{V_{cell}}{\hbar^D}\int_{BZ}\frac{d^Dk}{(2\pi)^D}e^{i\boldsymbol{k}\cdot\boldsymbol{R}/\hbar}\langle m|\nabla^2_{\boldsymbol{k}}|n\rangle, \tag{2-16}$$

Then, we are concerned with getting the gauge-invariant part

$$\Omega_I = \sum_{n,\mu}\left[\langle 0n|r_\mu^2|0n\rangle - \left[\sum_{Rm}\langle 0n|r_\mu|Rm\rangle\langle Rm|r_\mu|0n\rangle\right]\right]. \tag{2-17}$$

Different gauges produce bases with different spatial spreads [14]. While various methods exist to optimize the localization of WFs to use just one set of

them to describe the spatial properties of the system, the so-called Maximally Localized Wannier Functions (MLWFs), in this work our interest lies solely in the gauge-invariant component of their spread, as this is the quantity that is physically meaningful and experimentally accessible through the optical sum rule. Therefore, the choice of gauge, the construction of MLWFs or any treatment for $\tilde{\Omega}$ are not the main concern of this study.

2.2 Quantum metric

2.2.1 Quantum metric tensor

In this section, we formulate the quantum geometry of the valence band states and explicitly demonstrate its connection to the spread of WFs discussed in the previous section. Quantum geometry holds significant relevance in condensed matter physics, providing an understanding of various properties. The first notions of quantum metric were introduced in 1980 [1], which is formulated in the following manner. Consider a quantum state described by some parameter λ, the expansion can be expressed by

$$|\psi(\lambda + \delta\lambda)\rangle \approx |\psi(\lambda)\rangle + |\partial_\mu \psi(\lambda)\rangle \delta_\mu \lambda, \tag{2-18}$$

where the sum over repeated indices was assumed.
The norm of the difference between two neighboring states $|\psi(\lambda)\rangle$ and $|\psi(\lambda + \delta\lambda)\rangle$ is given by

$$|||\psi(\lambda + \delta\lambda)\rangle - |\psi(\lambda)\rangle||^2 = \langle \partial_\mu \psi(\lambda)|\partial_\nu \psi(\lambda)\rangle \delta_\mu \lambda \delta_\nu \lambda, \tag{2-19}$$

as only the real part survives, and knowing that there is symmetry in $\delta_\mu \lambda \delta_\nu \lambda$, then $\langle \partial_\mu \psi(\lambda)|\partial_\nu \psi(\lambda)\rangle$ can take its real and imaginary parts as $\gamma_{\mu\nu} = \gamma_{\nu\mu}$ and $\sigma_{\mu\nu} = -\sigma_{\nu\mu}$, respectively. So only the real part would survive, making

$$|||\psi(\lambda + \delta\lambda)\rangle - |\psi(\lambda)\rangle||^2 = \mathrm{Re}[\langle \partial_\mu \psi(\lambda)|\partial_\nu \psi(\lambda)\rangle] \delta_\mu \lambda \delta_\nu \lambda. \tag{2-20}$$

We define the tensor $Q_{\mu\nu} = \langle \partial_\mu \psi(\lambda)|\partial_\nu \psi(\lambda)\rangle$, to be analyzed separately. We see that any tensor of the form $Q_{\mu\nu} \to Q_{\mu\nu} - B_{\mu\nu}$ is useful for solving eq. (2-19), provided that $B_{\mu\nu}$ is antisymmetric. We can see that, due to the gauge dependence of the states $|\psi(\lambda)\rangle$, the tensor to be defined is of the form $T_{\mu\nu} = Q_{\mu\nu} - A_\mu [A_\nu]^\dagger$, where $A_\mu = \langle \psi(\lambda)|i\partial_\mu \psi(\lambda)\rangle$ is the **Berry connection**. This specific combination is not arbitrary. Under a gauge transformation, the wavefunction acquires a phase factor, which causes $Q_{\mu\nu}$ and A_μ to change, but $T_{\mu\nu}$ is unchanged. Therefore, this is the minimal and natural way to obtain a

gauge-invariant metric tensor from the derivatives of the quantum state. This gauge-invariant structure is known as **quantum metric tensor**. This tensor is expressed as

$$T_{\mu\nu} = \langle \partial_\mu \psi(\lambda) | \partial_\nu \psi(\lambda) \rangle - \langle \partial_\mu \psi(\lambda) | \psi(\lambda) \rangle \langle \psi(\lambda) | \partial_\nu \psi(\lambda) \rangle, \tag{2-21}$$

since the product $\langle \psi | \partial_\mu \psi \rangle$ is pure imaginary, it is possible to separate the quantum metric tensor into two parts:

$$\begin{aligned} g_{\mu\nu} =& \frac{1}{2} \langle \partial_\mu \psi(\lambda) | \partial_\nu \psi(\lambda) \rangle + \frac{1}{2} \langle \partial_\nu \psi(\lambda) | \partial_\mu \psi(\lambda) \rangle \\ & - \langle \partial_\mu \psi(\lambda) | \psi(\lambda) \rangle \langle \psi(\lambda) | \partial_\nu \psi(\lambda) \rangle \\ \Omega_{\mu\nu} =& i \left[\langle \partial_\mu \psi(\lambda) | \partial_\nu \psi(\lambda) \rangle - \langle \partial_\nu \psi(\lambda) | \partial_\mu \psi(\lambda) \rangle \right], \end{aligned} \tag{2-22}$$

so that $T_{\mu\nu} = g_{\mu\nu} - \frac{i}{2}\Omega_{\mu\nu}$, or that is equivalent, $g_{\mu\nu} = \mathrm{Re}[T_{\mu\nu}]$ and $\Omega_{\mu\nu} = -2\mathrm{Im}[T_{\mu\nu}]$ [2–4]. Then, the measure of the distance between two neighboring states $|\psi(\lambda)\rangle$ and $|\psi(\lambda + \delta\lambda)\rangle$ is given by

$$ds^2 = |\langle \psi(\lambda) | \psi(\lambda + \delta\lambda) \rangle|^2 = T_{\mu\nu} \delta\lambda^\mu \delta\lambda^\nu. \tag{2-23}$$

The term $\Omega_{\mu\nu}$ is called **Berry curvature**, which is responsible for phenomena such as Hall effects [6], and is related to electronic properties [5] and topological phases of matter [7, 8]. On the other hand, the real part of $T_{\mu\nu}$ is symmetric and corresponds to the **quantum metric** $g_{\mu\nu}$, which also arises equivalently from the expression $|\langle \psi(\lambda) | \psi(\lambda + \delta\lambda) \rangle| = 1 - \frac{1}{2} g_{\mu\nu} \delta\lambda^\mu \delta\lambda^\nu$. For solids, we use momentum space Hamiltonian and Bloch eigenstates to define this quantum metric, as we will see later.

The quantum metric can be related to various experimental measures [9–12]. For example, there are investigations that show how to relate the metric to optical responses by introducing a object called the quantum metric spectral function $g^d_{\mu\nu}(k, \omega)$ [5, 25, 31], where the superscript is introduced because the system is considered to be "dressed" by interactions, as could it be an environment with $T \neq 0$ K. For the case of a gapped material (our aim), known as those materials that exhibit a gap in their electronic structure, it is possible to relate the quantum metric spectral function, which integrates over frequency to the quantum metric, with the optical absorption rate [24].

In addition, it has also been found that the quantum metric is related to topological order. This is a type of order that represents a certain geometric property of the Bloch state in the momentum space, and depending on the dimension and symmetry of the system [2, 34]. This order can manifest itself through different physical phenomena. In systems characterized by a topological order derived from the integration of the Berry curvature into the

momentum space, the determinant of the quantum metric is related to these quantities [22,23,26]. In relation to the aforementioned, it has been found that in Dirac models, when the integration of a certain function with respect to the momentum results in a topological order, the modulus of that function is equal to the determinant of the quantum metric. This relationship has been called the metric-curvature correspondence [2, 5], which is useful in revealing the topological order through the excitation absorption rate measures mentioned above.

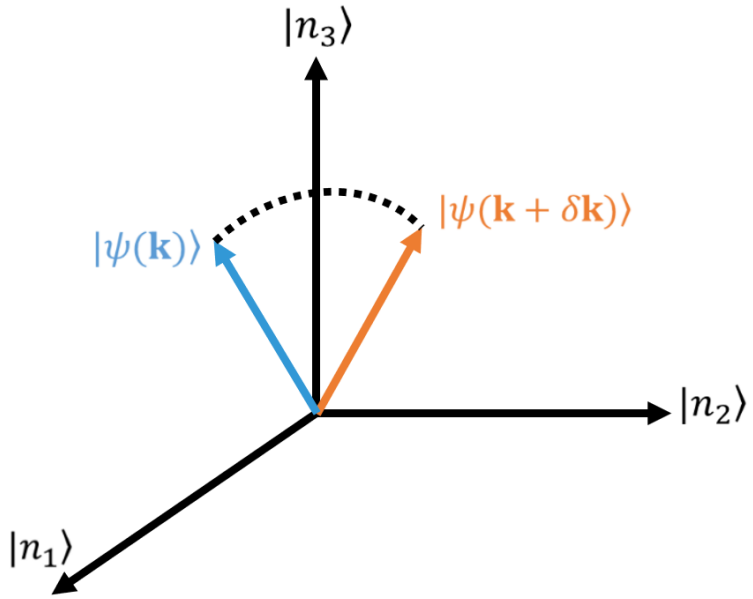

Figure 2.2: Representation of rotation of a unit vector $\psi(\boldsymbol{k})$ in the Hilbert space in some basis $|n_1\rangle$, $|n_2\rangle$ and $|n_3\rangle$ from $\boldsymbol{k}$ to $\boldsymbol{k}+\delta\boldsymbol{k}$.

To start our analysis in momentum space, we establish the parameter λ as momentum $\boldsymbol{k}$, then the quantum metric can be defined as follows

$$|\langle\psi(\boldsymbol{k})|\psi(\boldsymbol{k}+\delta\boldsymbol{k})\rangle| = 1 - \frac{1}{2}g_{\mu\nu}(\boldsymbol{k})\delta k^{\mu}\delta k^{\nu}. \tag{2-24}$$

Equation (2-24) indicates that if we take the modulus of a state $|\psi(\boldsymbol{k})\rangle$ that overlaps with itself at slightly different momentum and perform an expansion in terms of small displacement $\delta\boldsymbol{k}$, the result introduces a prefactor denoted by $g_{\mu\nu}(\boldsymbol{k})$, which is the quantum metric. A very intuitive picture that allows us to visualize this is Fig. 2.2, where we have the unit vector $|\psi(\boldsymbol{k})\rangle$ in the Hilbert space in some basis $|n_1\rangle$, $|n_2\rangle$ and $|n_3\rangle$. This vector is pointing in some direction, and when we move from $\boldsymbol{k}$ to $\boldsymbol{k}+\delta\boldsymbol{k}$, this unit vector will rotate in a different direction in the Hilbert space. If we now take the product between these two unit vectors, the result must be less than one. Hence, if an expansion is performed, the correction should give us the quantum metric.

Suppose the system has a gap and occupies N_- valence bands (including spin or

any other quantum number), then the fully antisymmetric many-body valence band Bloch state is given by

$$|u^{val}(\boldsymbol{k})\rangle = \frac{1}{\sqrt{N_-}}\epsilon^{n_1 n_2 \ldots n_{N_-}}|n_1\rangle|n_2\rangle \ldots |n_{N_-}\rangle, \tag{2-25}$$

where $|n_i\rangle = |n_i(\boldsymbol{k})\rangle$.
The main ingredient in our formalism is the quantum metric defined in equation (2-24) from the overlap of neighboring valence band states in the momentum space [1]

$$|\langle u^{val}(\boldsymbol{k})|u^{val}(\boldsymbol{k}+\delta\boldsymbol{k})\rangle| = 1 - \frac{1}{2}g_{\mu\nu}(\boldsymbol{k})\delta k^\mu \delta k^\nu, \tag{2-26}$$

which amounts to the expression [2, 24]

$$\begin{aligned} g_{\mu\nu}(\boldsymbol{k}) =& \frac{1}{2}\langle\partial_\mu u^{val}|\partial_\nu u^{val}\rangle + \frac{1}{2}\langle\partial_\nu u^{val}|\partial_\mu u^{val}\rangle \\ & - \langle\partial_\mu u^{val}|u^{val}\rangle\langle u^{val}|\partial_\nu u^{val}\rangle \\ =& \frac{1}{2}\sum_{nm}[\langle\partial_\mu n|m\rangle\langle m|\partial_\nu n\rangle + \langle\partial_\nu n|m\rangle\langle m|\partial_\mu n\rangle], \end{aligned} \tag{2-27}$$

where we denote $|m\rangle$ as a conduction band state and $|n\rangle$ as the valence band state. The closure relation reads $\sum_{n\in v}|n\rangle\langle n| + \sum_{m\in c}|m\rangle\langle m| = Q_- + Q_+ = I$ [5].

2.2.2 Fidelity number

The key quantum geometrical quantity that is related to the spread of WFs is the momentum integral of the quantum metric [13, 14, 23].

$$\mathcal{G}_{\mu\nu} = \int_{BZ}\frac{d^D k}{(2\pi)^D}g_{\mu\nu}(\boldsymbol{k}), \tag{2-28}$$

and we call it the **fidelity number**. The BZ in a dimension D can be considered as a torus T^D from a differential geometry perspective. It can be inferred that by the integral of the quantum metric over momentum space on the torus T^D, given in eq. (2-27). It represents the average distance between neighboring Bloch states, $|\psi(\boldsymbol{k})\rangle$ and $|\psi(\boldsymbol{k}+\delta\boldsymbol{k})\rangle$; this quantity may be considered an intrinsic property of the quantum geometry.

The momentum integration of the quantum metric spectral function gives us a term called the fidelity number spectral function $\mathcal{G}^d_{\mu\nu}(\omega)$. The frequency integral gives the dressed fidelity number

$$\mathcal{G}^d_{\mu\nu} = \int_0^\infty d\omega\mathcal{G}^d_{\mu\nu}(\omega),\ \ \mathcal{G}^d_{\mu\nu}(\omega) = \int_{BZ}\frac{d^D k}{(2\pi)^D}g^d_{\mu\nu}(\boldsymbol{k},\omega), \tag{2-29}$$

which is the key ingredient to link the quantum geometry to the optical absorption power, as we shall see below for 3D and 2D materials. We call this

quantity $\mathcal{G}^d_{\mu\mu}$ the fidelity number because it is dimensionless in 2D. Although in 3D it has the unit of momentum, it can be trivially multiplied by $V_{cell}^{1/3}/\hbar$ to make it dimensionless, and hence we stick with this nomenclature, in the form $\mathcal{G}^d_{\mu\mu} \to \mathcal{G}^d_{\mu\mu}\left(V_{cell}^{1/D}/\hbar\right)^{D-2}$.

We can express this quantity in real space through this projection formalism to define a **fidelity marker** at each lattice site, which allows us to study, for example, the influence of impurities in real space on the quantum geometric properties [24]. This latter concept will be necessary in the Sec. 3.2.3.

2.2.3 Experimental relations

To link these geometrical quantities with experimentally measurable data, it is practical to introduce a quantum metric spectral function $g^d_{\mu\mu}(\boldsymbol{k},\omega)$ to define the real part of longitudinal optical conductivity at momentum $\boldsymbol{k}$, frequency ω and polarization $\hat{\boldsymbol{\mu}}$ [5, 24, 25].

$$\begin{aligned}\sigma_{\mu\mu}(\boldsymbol{k},\omega) &= \sum_{l<l'} \frac{\pi}{V_{cell}\hbar\omega}\langle l|\hat{j}_\mu|l'\rangle\langle l'|\hat{j}_\mu|l\rangle[f(\varepsilon^{\boldsymbol{k}}_l) - f(\varepsilon^{\boldsymbol{k}}_{l'})]\delta\left(\omega + \frac{\varepsilon^{\boldsymbol{k}}_l}{\hbar} - \frac{\varepsilon^{\boldsymbol{k}}_{l'}}{\hbar}\right) \\ &= \frac{\pi e^2}{V_{cell}}\hbar\omega g^d_{\mu\mu}(\boldsymbol{k},\omega),\end{aligned} \tag{2-30}$$

where $f(\varepsilon^{\boldsymbol{k}}_l)$ is the Fermi distribution function at the eigenenergy $\varepsilon^{\boldsymbol{k}}_l$ and $\hat{j}_\mu$ represents the μ-th component of the current operator (we obtain this relation by Kubo formula and Matsubara frequency summations [25]). As noted previously, the superscript d indicates "dressed", since the optical conductivity formalism incorporates finite temperature and many-body interactions. The frequency integral of $g^d_{\mu\mu}(\boldsymbol{k},\omega)$ gives the dressed quantum metric $g^d_{\mu\mu}(\boldsymbol{k}) = \int_0^\infty d\omega g^d_{\mu\mu}(\boldsymbol{k},\omega)$ as has been pointed out previously [5, 26–29]. In the zero temperature and non-interacting limit $\lim_{T\to 0} g^d_{\mu\mu}(\boldsymbol{k}) = g_{\mu\mu}(\boldsymbol{k})$, the frequency integration recovers to the expression given by eq. (2-28).

It is important to note that the zero temperature limit is appropriate for describing the optical properties of semiconductors at room temperature in practice, since the band gap is typically much larger than the thermal energy at room temperature. Therefore, the occupation of states is well-approximated by the zero temperature Fermi distribution. In the following calculations, we will neglect the Fermi distribution factor and simply use the zero temperature formula to compare with experimental data.

The optical conductivity measured in a real experiment corresponds to the momentum integration of $\sigma_{\mu\mu}(\boldsymbol{k},\omega)$ over the BZ of volume $V_{BZ} =$

$(2\pi)^D/V_{cell}$

$$\begin{aligned}\sigma_{\mu\mu}(\omega) &= \int \frac{d^D k}{\hbar^D V_{BZ}} \sigma_{\mu\mu}(\boldsymbol{k},\omega) \\ &= \frac{\pi e^2}{\hbar^{D-1}}\omega \int \frac{d^D k}{(2\pi)^D} g^d_{\mu\mu}(\boldsymbol{k},\omega) \equiv \frac{\pi e^2}{\hbar^{D-1}}\omega \mathcal{G}^d_{\mu\mu}(\omega),\end{aligned} \tag{2-31}$$

leading to the dressed fidelity number spectral function $\mathcal{G}^d_{\mu\mu}(\omega)$ at polarization $\hat{\mu}$.

2.3 Relating quantum geometry to the spread of Wannier functions

We proceed by elaborating on a connection between the fidelity number and the spread of the valence band WFs compared to our aforementioned objective of equation (2-29), defined by Refs. [13, 14] in equation (2-13).

The main goal of the present work is to propose an experimental protocol to determine Ω_I based on its relation with the fidelity number $\mathcal{G}_{\mu\mu}$, and the connection of the latter with the longitudinal optical conductivity $\sigma_{\mu\mu}(\omega)$ according to equations (2-29) and (2-31). This equivalence can be seen by considering the identities

$$\begin{aligned}\langle r^2\rangle_n &= \frac{V_{cell}}{\hbar^{D-2}} \int \frac{d^D k}{(2\pi)^D} \sum_\mu \langle \partial_\mu n | \partial_\mu n\rangle \\ \langle \boldsymbol{R} n' | \hat{r}_\mu | \boldsymbol{0} n\rangle &= \frac{V_{cell}}{\hbar^{D-1}} \int \frac{d^D k}{(2\pi)^D} \langle n' | i\partial_\mu | n\rangle e^{i\boldsymbol{k}\cdot\boldsymbol{R}/\hbar},\end{aligned} \tag{2-32}$$

from which Ω_I can be written as

$$\begin{aligned}\Omega_I =& \frac{V_{cell}}{\hbar^{D-2}} \int \frac{d^D \boldsymbol{k}}{(2\pi)^D} \sum_\mu \sum_n \left[\langle \partial_\mu n | \partial_\mu n\rangle - \sum_{n'} \langle \partial_\mu n | n'\rangle \langle n' | \partial_\mu n\rangle \right] \\ =& \frac{V_{cell}}{\hbar^{D-2}} \mathrm{Tr}\mathcal{G}_{\mu\nu} = \frac{V_{cell}}{\hbar^{D-2}} \sum_\mu \mathcal{G}_{\mu\mu},\end{aligned} \tag{2-33}$$

indicating that the gauge-invariant part of the spread of valence band Wannier states is equivalent to the trace of fidelity number (tensor). Thus, the quantum metric formalism developed in Sec. 2.2 linking the fidelity number to optical conductivity can be particularly useful for extracting Ω_I experimentally, as we shall see in the following sections devoted to particular 3D and 2D systems.

3
Spread of Wannier functions in different systems

3.1
Extracting the spread of Wannier functions in 3D systems from dielectric function

Assume an oscillatory electric field whose spatial profile changes on a length scale far exceeding the lattice constant a. Under this long-wavelength condition, the complex dielectric function and the optical conductivity are related through [30]

$$\varepsilon(\omega) = \mu_r \varepsilon_r + i\frac{\mu_r \tilde{\sigma}(\omega)}{\varepsilon_0 \omega}, \tag{3-1}$$

where ε_0 is the vacuum permittivity, ε_r is the relative dielectric constant, and μ_r is the relative magnetic permeability, which is practically unity for most insulators. The real part of the complex optical conductivity $\tilde{\sigma}(\omega)$ is $\sigma_{\mu\mu}(\omega)$ in eq. (2-31) after averaging over the three crystalline directions $\boldsymbol{\mu}$. Hence, the imaginary component of the dielectric function, $\mathrm{Im}[\varepsilon(\omega)]$, is governed by the real part of the optical conductivity, and can be connected to the fidelity number spectral function via

$$\mathrm{Im}[\varepsilon(\omega)] = \frac{1}{3}\sum_{\mu}\frac{\sigma_{\mu\mu}(\omega)}{\varepsilon_0\omega} = \frac{\pi e^2}{\varepsilon_0 \hbar^2} \times \frac{1}{3}\sum_{\mu}\mathcal{G}^d_{\mu\mu}(\omega), \tag{3-2}$$

where the factor of $1/3$ is explained below. Consequently, the dressed fidelity number and the spread of valence band WFs are determined directly by frequency/energy integrals of $\mathrm{Im}[\varepsilon(\omega)]$

$$\frac{1}{3}\sum_{\mu}\mathcal{G}^d_{\mu\mu} = \frac{\varepsilon_0 \hbar}{\pi e^2}\int_0^{\infty} d(\hbar\omega)\mathrm{Im}[\varepsilon(\omega)] \tag{3-3}$$

$$\Omega_I = \lim_{T\to 0}\frac{V_{cell}\varepsilon_0}{\pi e^2} \times 3\int_0^{\infty} d(\hbar\omega)\mathrm{Im}[\varepsilon(\omega)]. \tag{3-4}$$

This equation is the cornerstone of our three-dimensional formulation, providing a concrete experimental protocol for extracting Ω_I.

3.1.1
Applications to common semiconductors and topological insulators

Extensive experimental records on the frequency dependence of the dielectric function exist for many semiconductor compounds. Nevertheless, a

few subtleties arise when one wants to deduce Ω_I from those data, and we discuss them below.

First, in most optical setups the sample is polycrystalline and the incident beam is unpolarized; this situation is equivalent to irradiating a perfect single crystal with light whose polarization is random. Therefore, we model the incident electric field as

$$\boldsymbol{E} = E_0(\sin\theta\cos\phi, \sin\theta\sin\phi, \cos\theta)\cos\omega t, \tag{3-5}$$

which is uniformly distributed over the the solid angle element $\sin\theta d\theta d\phi$.

Writing the induced electric current at frequency ω as $j_\mu = \sigma_{\mu\nu}E_\nu$, the absorbed power density reads $W_a(\omega,\theta,\phi) = \sum_\mu \langle j_\mu(\omega,t)E_\mu(\omega,t)\rangle_t = \sum_\mu j_\mu(\omega)E_\mu(\omega)/2 = \sum_{\mu\nu}\sigma_{\mu\nu}(\omega)E_\mu(\omega)E_\nu(\omega)/2$, where the prefactor $1/2$ stems from the time average $\langle\cos^2\omega t\rangle_t = 1/2$, because both the current and field oscillate harmonically at frequency ω. Averaging this absorption power over all directions of incidence yields

$$\begin{aligned}\overline{W}_a(\omega) &= \frac{1}{4\pi}\int_0^{2\pi} d\phi \int_0^{\pi} d\theta \sin\theta \frac{1}{2}\sum_\mu j_\mu(\omega)E_\mu(\omega) \\ &= \frac{1}{2}\left(\frac{1}{3}\sum_\mu \sigma_{\mu\mu}(\omega)\right)E_0^2 \equiv \frac{1}{2}\overline{\sigma}(\omega)E_0^2,\end{aligned} \tag{3-6}$$

thus the measurements provide the directionally averaged optical conductivity $\overline{\sigma}(\omega) = \sum_\mu \sigma_{\mu\mu}(\omega)/3$ and therefore the averaged dielectric function $\mathrm{Im}[\varepsilon(\omega)]$. Because the Ω_I in eq. (3-4) requires a sum over the three crystalline axes, one must multiply the experimentally obtained dielectric function by a factor of three, i.e., employ $3\mathrm{Im}[\varepsilon(\omega)]$.

Second, in gapped materials, optical absorption is not limited to direct valence-to-conduction interband transitions; excitonic resonances can also appear. We suggest that, when one integrates the measured spectra, any distinct peaks that occur inside the fundamental gap should be excluded, as they originate from bound electron-hole pairs rather than from free-carrier excitations. A case like this is elaborated in Sec. 3.2.3 for TMD materials.

Third, the optical measurements usually report the dielectric response as a function of photon energy (eV) rather than angular frequency (ω). Accordingly, we recast the frequency integral as

$$\int_0^\infty d(\hbar\omega)\mathrm{Im}[\varepsilon(\omega)] = \int_0^\infty d(\mathrm{eV})\mathrm{Im}[\varepsilon(\mathrm{eV})] = \nu \times \mathrm{eV}, \tag{3-7}$$

where ν is a dimensionless factor obtained from the experimental curve, and the eV units come from the integration over the photon energy. Inserting this factor with the factor of 3 derived earlier into eq. (3-4) gives

$$\begin{aligned}\Omega_I &= \lim_{T\to 0} \frac{V_{cell}\varepsilon_0}{\pi e^2}\text{eV} \times 3\nu \\ &= \lim_{T\to 0} \frac{V_{cell}}{\mathring{A}} \times 1.7591 \times 10^{-3} \times 3\nu \\ \text{Tr}\mathcal{G}_{\mu\nu} &= \lim_{T\to 0} \frac{\hbar}{\mathring{A}} \times 1.7591 \times 10^{-3} \times 3\nu,\end{aligned} \tag{3-8}$$

which furnish extremely simple working formulas for extracting Ω_I and $\text{Tr}\mathcal{G}_{\mu\nu}$ directly from optical spectra. Because typical semiconductor band gaps greatly exceed k_BT at room temperature, the limit $T \to 0$ K in eq. (3-8) is effectively satisfied in ordinary conditions.

Combining the spread Ω_I and V_{cell}, one may form the dimensionless ratio $\Omega_I^{3/2}/V_{cell}$ as a measure of insulating character of the material. Table 3.1 illustrates this procedure: digitized dielectric function data for Si and Ge (conventional semiconductors) and Bi_2Te_3 (3D topological insulator) from Refs. [17,18] and [19] are integrated to obtain ν. Then, the eq. (3-8) yields Ω_I. The outcome points to a markedly more extended Wannier function in Bi_2Te_3 than Si or Ge, consistent with its much narrower gap (~ 0.4 eV compared to ~ 2 eV). Such a small gap places Bi_2Te_3 closer to the verge of a topological band-inversion transition, a regime where Wannier functions are expected to acquire longer spatial range [24].

Table 3.1: Volume of the unit cell V_{cell}, frequency-integration ν of the imaginary part of dielectric function, trace of the fidelity number $\text{Tr}\, G_{\mu\nu}$, spread of the valence-band WFs Ω_I, the dimensionless ratio $\Omega_I^{3/2}/V_{\text{cell}}$ and the band gap obtained from experimental data for semiconductors Si and Ge, and topological insulator Bi_2Te_3.

Mat.	$\boldsymbol{V_{\text{cell}}}$ (Å^3)	$\boldsymbol{\nu}$	$\textbf{Tr}\, \boldsymbol{G_{\mu\nu}}$ ($\hbar$/Å)	$\boldsymbol{\Omega_I}$ (Å^2)	$\boldsymbol{\Omega_I^{3/2}/V_{\text{cell}}}$	$\boldsymbol{\Delta}$ (eV)
Si	160.1	80.6	0.425	68.1	3.51	1.12
Ge	181.3	87.0	0.459	83.24	4.19	0.66
Bi_2Te_3	545.3	141.6	0.747	407.48	15.08	0.15

3.2 Detecting the spread of Wannier functions in 2D systems by absorbance

Imagine a 2D material subject to a linearly polarized time-harmonic electric field $E_\mu(\omega, t) = E_0 \cos\omega t$. This drive induces a current $j_\mu(\omega, t) = \sigma_{\mu\mu}(\omega)E_0 \cos\omega t$. The optical-power density absorbed at frequency ω and polarization μ is therefore

$$\begin{aligned} W_a^{\mu}(\omega) &= \langle j_\mu(\omega,t)E_\mu(\omega,t)\rangle_t = \frac{1}{2}\sigma_{\mu\mu}(\omega)E_0^2 \\ &= \frac{\pi e^2}{2\hbar}E_0^2\omega\mathcal{G}^d_{\mu\mu}(\omega). \end{aligned} \tag{3-9}$$

For an incident plane wave, the incoming power flux per unit area is $W_i = c\varepsilon_0 E_0^2/2$. Thus, the absorbance at polarization μ is [32]

$$\mathcal{O}_\mu(\omega) = \frac{W_a(\omega)}{W_i} = 4\pi^2\alpha\omega\mathcal{G}^d_{\mu\mu}(\omega)\mid_{2D}, \tag{3-10}$$

with $\alpha = e^2/4\pi\varepsilon_0\hbar c \approx 1/137$ as the fine-structure constant. Hence, the dressed fidelity number spectral function $\mathcal{G}^d_{\mu\mu}(\omega)$ can be read directly from experiment

$$\mathcal{G}^d_{\mu\mu}(\omega)\mid_{2D} = \frac{1}{4\pi\omega}\left[\frac{\mathcal{O}_\mu(\omega)}{\pi\alpha}\right], \tag{3-11}$$

following the discussion in Sec. 2.2, in the zero temperature and non-interacting limit $\lim_{T\to 0}\mathcal{G}^d_{\mu\nu}(\omega) = \mathcal{G}_{\mu\nu}(\omega)$. So, from equation (2-33), the gauge-invariant spread is simply given as

$$\begin{aligned} \Omega_I &= A_{cell}\mathrm{Tr}\mathcal{G}_{\mu\nu} = A_{cell}\int_0^\infty d\omega \mathrm{Tr}\mathcal{G}_{\mu\nu}(\omega) \\ &= \lim_{T\to 0} A_{cell}\sum_\mu \int_0^\infty d\omega \frac{1}{4\pi\omega}\left[\frac{\mathcal{O}_\mu(\omega)}{\pi\alpha}\right]. \end{aligned} \tag{3-12}$$

Thus the ratio $\Omega_I/A_{cell} = \mathrm{Tr}\mathcal{G}_{\mu\nu}$−which characterizes how insulating is the material−comes straight from the trace of fidelity number.

If the absorbance is measured with unpolarized light or on a polycrystalline sample, the angle-averaged absorption power becomes

$$\overline{W}_a = \int_0^{2\pi}\frac{d\phi}{2\pi}W_a(\phi) = \frac{1}{2}\left(\frac{1}{2}\sigma_{xx}(\omega) + \frac{1}{2}\sigma_{yy}(\omega)E_0^2\right) \equiv \frac{1}{2}\overline{\sigma}(\omega)E_0^2, \tag{3-13}$$

so that $\sum_\mu \mathcal{O}_\mu(\omega) = 2\overline{O}(\omega)$. Inserting this into eq. (3-12) just gives

$$\Omega_I = \lim_{T\to 0} A_{cell}\int_0^\infty d\omega \frac{1}{2\pi\omega}\left[\frac{\overline{\mathcal{O}}(\omega)}{\pi\alpha}\right] = A_{cell}\mathrm{Tr}\mathcal{G}_{\mu\nu}. \tag{3-14}$$

Equations (3-12)–(3-14) therefore supply a practical, experiment-based recipe for determining the gauge-invariant spread of WFs and the trace of fidelity-number, enabling direct comparison with first-principles or tight-binding predictions. The subsequent sections apply this protocol to monolayer graphene with ISOC, twisted bilayer graphene, and several transition-metal dichalcogenides to establish realistic scales for Ω_I in representative 2D gapped materials.

3.2.1 Graphene with ISOC

We start with a nearest-neighbor tight-binding description of graphene that explicitly includes ISOC, a key ingredient for the quantum spin Hall effect (QSHE) in the Kane-Mele model [36, 37]. Taking the lattice constant of the honeycomb lattice as the unit of length $a_L = 1$, we define the lattice vectors as [20]

$$\begin{aligned} \boldsymbol{R}_1 &= (1,0)a_L, \quad \boldsymbol{R}_2 = \left(-\frac{1}{2}, \frac{\sqrt{3}}{2}\right) a_L, \\ \boldsymbol{R}_3 &= \left(-\frac{1}{2}, -\frac{\sqrt{3}}{2}\right) a_L, \end{aligned} \tag{3-15}$$

as can be visualized in Fig. 3.1.

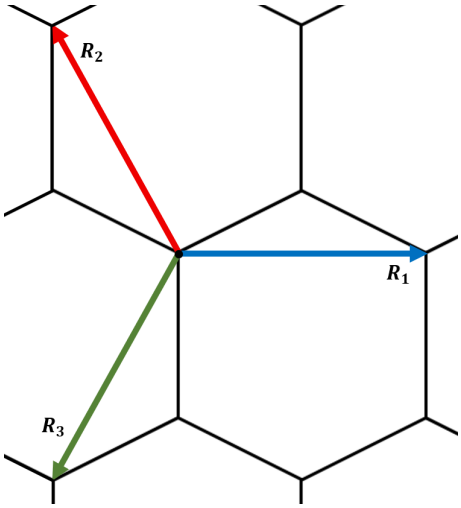

Figure 3.1: Monolayer graphene and its lattice vectors, as defined in eq. (3-15)

The second-quantized Hamiltonian is written as $\mathcal{H} = \sum_{\boldsymbol{q}} \psi^\dagger_{\boldsymbol{q}} H(\boldsymbol{q}) \psi_{\boldsymbol{q}}$ with the spinor basis $\psi^\dagger_{\boldsymbol{q}} = \{c^\dagger_{A\boldsymbol{q}\uparrow}, c^\dagger_{B\boldsymbol{q}\uparrow}, c^\dagger_{A\boldsymbol{q}\downarrow}, c^\dagger_{B\boldsymbol{q}\downarrow}\}$, where $c^\dagger_{X\boldsymbol{q}\sigma}$ is the electron creation operator at momentum $\boldsymbol{q}$ (with respect to the center of BZ), sublattice $X = \{A, B\}$, and spin $\sigma = \{\uparrow, \downarrow\}$. In this basis, the 4×4 Hamiltonian takes the form

$$\begin{aligned} H(\boldsymbol{q}) &= \begin{pmatrix} \lambda_I f_I & -t f_{orb} & 0 & 0 \\ -t f^*_{orb} & -\lambda_I f_I & 0 & 0 \\ 0 & 0 & -\lambda_I f_I & -t f_{orb} \\ 0 & 0 & -t f^*_{orb} & \lambda_I f_I \end{pmatrix} \\ f_{orb}(\boldsymbol{q}) &= 1 + e^{i\boldsymbol{q}\cdot\boldsymbol{R}_2/\hbar} + e^{-i\boldsymbol{q}\cdot\boldsymbol{R}_3/\hbar} \\ f_I(\boldsymbol{q}) &= -\frac{2}{3\sqrt{3}} \sum_{i=1}^{3} \sin(\boldsymbol{q}\cdot\boldsymbol{R}_i/\hbar). \end{aligned} \tag{3-16}$$

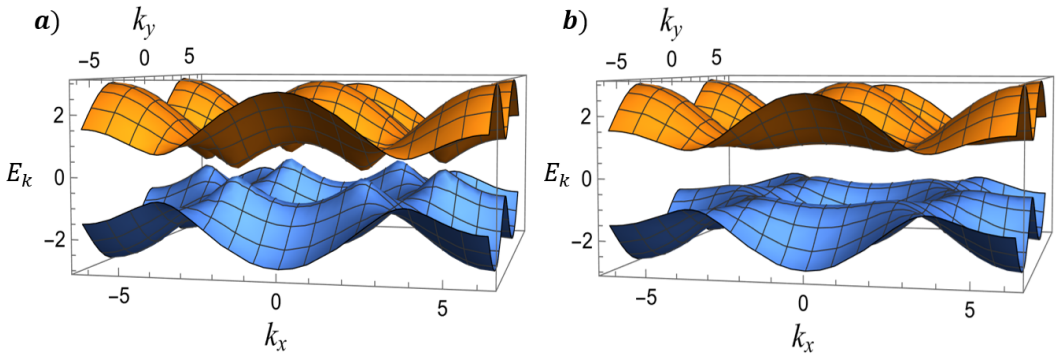

Figure 3.2: Energy dispersion of graphene defined by the Hamiltonian of eq. (3.16) (a) $\lambda_I/t = 0.1$ and (b) $\lambda_I/t = 0.8$, to visualize the band separation due to the ISOC strength.

The hopping amplitudes t and λ_I measure, respectively, the nearest-neighbor hopping and the ISOC strength. The corresponding band structure hosts Dirac points at

$$\frac{\boldsymbol{K}}{\hbar/a_L} = \left(\frac{4\pi}{3}, 0\right), \quad \frac{\boldsymbol{K'}}{\hbar/a_L} = \left(-\frac{4\pi}{3}, 0\right), \tag{3-17}$$

which will play a crucial role in the optical-response analysis, as we can see later.

3.2.1.1 Quantum geometry induced by ISOC

We observe that the Hamiltonian in eq. (3-16) can be written in a Dirac form. A convenient representation with 4×4 Dirac matrices (see eq. (B.2) of Ref. [33]) is

$$\Gamma_{1\sim5} = (\hat{s}_1 \otimes \hat{\sigma}_3, \hat{s}_2 \otimes \hat{\sigma}_3, \hat{s}_0 \otimes \hat{\sigma}_1, \hat{s}_0 \otimes \hat{\sigma}_2, \hat{s}_3 \otimes \hat{\sigma}_3), \tag{3-18}$$

where $\hat{s}_\alpha$ and $\hat{\sigma}_\alpha$ are the Pauli matrices acting in the spin space $\{\uparrow, \downarrow\}$ and the sublattice space $\{A, B\}$, respectively. Using this set, the Hamiltonian of eq. (3-16) can be expressed as a linear combination of the Γ-matrices $(\Gamma_3, \Gamma_4, \Gamma_5)$

$$\begin{aligned} &H(\boldsymbol{q}) = \boldsymbol{d} \cdot \boldsymbol{\Gamma} = d_3\Gamma_3 + d_4\Gamma_4 + d_5\Gamma_5 \\ &(d_3, d_4) = -t(\mathrm{Re}, \mathrm{Im}) f_{orb}(\boldsymbol{q}), \;\; d_5 = \lambda_I f_I(\boldsymbol{q}). \end{aligned} \tag{3-19}$$

Defining the unit vector [34]

$$\boldsymbol{n}(\boldsymbol{q}) \equiv \boldsymbol{d}/|\boldsymbol{d}| = (\tilde{n}_3, \tilde{n}_4, \tilde{n}_5), \tag{3-20}$$

where $|\boldsymbol{d}| = d = \sqrt{\sum_i |d_i|^2}$. Explicitly expanding the momentum around the two Dirac points, we set

$$\boldsymbol{q} = \boldsymbol{K}^{(\prime)} + \boldsymbol{k}, \tag{3-21}$$

so that the five-component vector $\boldsymbol{d} = (d_1, d_2, d_3, d_4, d_5)$ becomes to linear order in the small deviation $\boldsymbol{k}$

$$\begin{aligned} \boldsymbol{K} &: \boldsymbol{d} = (0, 0, v_F k_x, v_F k_y, \lambda_I) \\ \boldsymbol{K}' &: \boldsymbol{d} = (0, 0, -v_F k_x, v_F k_y, -\lambda_I), \end{aligned} \tag{3-22}$$

where $v_F = \sqrt{3} t a_L / 2\hbar \sim 10^6$ m/s is the Fermi velocity of graphene. We next evaluate the quantum metric of graphene in the presence of ISOC.
For the Dirac-form Hamiltonian in eq. (3-19), the quantum metric can be written as [2]

$$g_{\mu\nu}(\boldsymbol{q}) = \left(\frac{N}{8}\right) \partial_\mu \boldsymbol{n}(\boldsymbol{q}) \cdot \partial_\nu \boldsymbol{n}(\boldsymbol{q}), \tag{3-23}$$

with $N = 4$ for the dimension of the Hamiltonian, and $\partial_\mu = \partial/\partial q_\mu$ is the corresponding momentum derivative. This yields

$$g_{\mu\nu} = \frac{1}{2d^2} \left\{ \sum_{i=3}^{5} \partial_\mu d_i \partial_\nu d_i - \partial_\mu d \partial_\nu d \right\}, \tag{3-24}$$

using the expression in eq. (3-22) close to valleys, one obtains

$$\begin{aligned} g_{xx} &= \frac{1}{2d^4} [v_F^2 \lambda_I^2 + v_F^4 k_y^2] \\ g_{yy} &= \frac{1}{2d^4} [v_F^2 \lambda_I^2 + v_F^4 k_x^2] \\ g_{xy} &= -\frac{v_F^4 k_x k_y}{2d^4}. \end{aligned} \tag{3-25}$$

Employing either valley and eq. (3-24), the low frequency parts of the fidelity number spectral function, eq. (2-29) and the absorbance, eq. (3-10), behave as in Chern insulators [31]. Explicitly, it gives the following fidelity number spectral function

$$\mathcal{G}^d_{\mu\mu}(\omega) = \int k \mathrm{d}k \int \frac{\mathrm{d}\theta}{8\pi d^4} \left[v_F^2 \lambda_I^2 + v_F^2 (k^2 - k_\mu^2) \right] (f(-d) - f(d)) \delta(\omega - \frac{2d}{\hbar}), \tag{3-26}$$

which yields the results

$$\begin{aligned} \mathcal{G}^d_{\mu\mu}(\omega) &= \left[\frac{1}{4\pi\omega} + \frac{\lambda_I^2}{\pi \hbar^2 \omega^3} \right] Z(\omega)|_{\omega \geq 2\lambda_I/\hbar} \\ \frac{\mathcal{O}_\mu(\omega)}{\pi\alpha} &= \left[1 + \frac{4\lambda_I^2}{\hbar^2\omega^2} \right] Z(\omega)|_{\omega \geq 2\lambda_I/\hbar} \\ Z(\omega) &= \left[f\left(-\frac{\hbar\omega}{2}\right) - f\left(\frac{\hbar\omega}{2}\right) \right], \end{aligned} \tag{3-27}$$

and f is the Fermi distribution. In Fig. 3.3 we plot these results for $\lambda_I = 12$ μeV ≈ 0.1 K and different values of temperature. Because $d = \sqrt{v_F^2 k^2 + \lambda_I^2} \geq \hbar\omega/2$, photons with $\omega < 2\lambda_I/\hbar$ cannot be absorbed; the $\delta-$function in eq. (3-26) enforces the threshold. Considering the lowest value when $k = 0$,

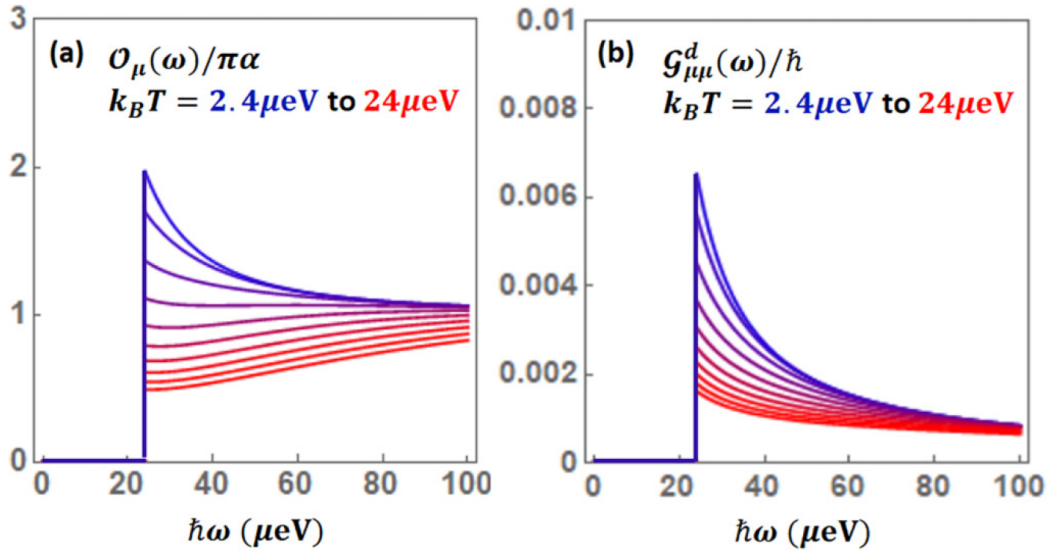

Figure 3.3: (a) The low frequency absorbance $\mathcal{O}_\mu(\omega)$ and (b) the fidelity number spectral function $\mathcal{G}^d_{\mu\mu}(\omega)$ computed for an arbitrary polarization direction $\hat{\mu}$ considering the ISOC strength $\lambda_I = 12$ μeV and orbital hopping amplitude $t = 2.8$ eV. Results are presented for several temperature values (solid lines with distinct colors) ranging from $k_BT = 2.4$ μeV ≈ 0.02 K up to 24 μeV ≈ 0.2 K.

and even lower values of ω we deduce that there is no light absorption, and $\mathcal{G}^d_{\mu\mu}(\omega < 2\lambda_I/\hbar) = 0$.

Our study reveals that ISOC, characterized by the parameter λ_I, suppresses the optical absorption in graphene at photon energies below the ISOC gap ($\hbar\omega < 2\lambda_I$), a range that—for a realistic λ_I—lies in the microwave domain. When the temperature is low enough that $k_BT \ll 2\lambda_I$, the same SOC interaction boosts absorption of light at the band edge ($\hbar\omega \approx 2\lambda_I$). Strikingly, in the zero temperature limit and for photons with energy exactly $2\lambda_I$, the absorbance reaches twice the topologically protected value, identical to that of pristine graphene and independent of the light polarization ($\mathcal{O}_\mu/\pi\alpha = 2$).

These distinctive spectral signatures suggest that λ_I can, in principle, be extracted experimentally—provided the sample is measured at low enough temperature and the Fermi level lies inside the gap. At higher temperatures, thermal broadening of the Fermi distribution diminishes the absorption, as illustrated in Fig. 3.3. To quantify the effect, we evaluate the fidelity number at $T \to 0$ using the full tight–binding Hamiltonian (eq. 3-16) and a realistic $\lambda_I \approx 12$ μeV. The calculations yields $G^d_{xx} = 1.08$ and $G^d_{yy} = 1.28$, indicating about a 20% anisotropy between zigzag and armchair directions. The resulting spread of WFs is $\Omega_I = 2.36 A_{cell} \approx 2.36 \times (\sqrt{3}/2) a_L^2$, only modestly larger than a single unit cell area, underscoring the internal consistency of the tight-binding model.

3.2.2 Twisted bilayer graphene (TBG)

Let us now consider TBG with a twist angle close to $\sim 1^o$, a system renowned for its phase diagram, including emergent superconductivity [38]. The physical properties of TBG are largely governed by the presence of flat bands and the associated Moiré patterns. These features not only give rise to unconventional superconducting behavior, as suggested by recent theoretical and experimental studies, but also strongly influence the quantum metric and the optical response offered by this material.

Within our approach, we calculate the spectral function fidelity number of TBG, focusing on the impact of flat bands on the absorption of light in the millimeter-wave region. The narrow bandwidth covered by these flat bands, typically spanning a few meV, and the quantum metric therein have been proposed to be related to the superfluid stiffness [9,10,39–41], highlighting the unique role of quantum geometry in determining the observable properties of TBG.

In the model given by Bistritzer and MacDonald [48], there is a set of magic angles $\theta \approx 1.05^o, 0.5^o, 0.35^o, 0.24^o$ and 0.2^o, but in practice only the first one has been observed [38], so we focus our attention on angles close to that value. In the model given by Bennett et. al. [21], they take into account the **atomic relaxation** (minimization of the energy of system due to a rearrangement of atoms) [47], and a magic range is defined between $0.91^o \leq \theta \leq 1.04^o$, where the band width is minimized, but the bands are never perfectly flat. We will use this model to explain the topological properties of the TBG and calculate the spread of the WFs.
Given the Moiré period a_{sc} (which acts as the lattice parameter of the Moiré superlattice), we define the vectors

$$\begin{aligned}
&\boldsymbol{a}_1 = a_{sc}\hat{\boldsymbol{x}}, \;\; \boldsymbol{a}_2 = a_{sc}\left(\frac{1}{2}\hat{\boldsymbol{x}} + \frac{\sqrt{3}}{2}\hat{\boldsymbol{y}}\right) \\
&\boldsymbol{a}_3 = a_{sc}\left(-\frac{1}{2}\hat{\boldsymbol{x}} + \frac{\sqrt{3}}{2}\hat{\boldsymbol{y}}\right), \;\; \boldsymbol{b}_1 = a_{sc}\left(\frac{1}{2}\hat{\boldsymbol{x}} + \frac{1}{2\sqrt{3}}\hat{\boldsymbol{y}}\right) \\
&\boldsymbol{b}_2 = a_{sc}\left(-\frac{1}{2}\hat{\boldsymbol{x}} + \frac{1}{2\sqrt{3}}\hat{\boldsymbol{y}}\right), \;\; \boldsymbol{b}_3 = -a_{sc}\frac{1}{\sqrt{3}}\hat{\boldsymbol{y}},
\end{aligned} \tag{3-28}$$

where the A vectors $(\boldsymbol{a}_1, \boldsymbol{a}_2, \boldsymbol{a}_3)$ join the vertices and the B vectors $(\boldsymbol{b}_1, \boldsymbol{b}_2, \boldsymbol{b}_3)$ join the middle of the triangles in the Moiré pattern. For calculations involving the electronic bands in TBG, it is often assumed−at least as a first approximation−that the two graphene layers are rigid and simply overlaid, preserving the individual honeycomb structures of each sheet. However, in re-

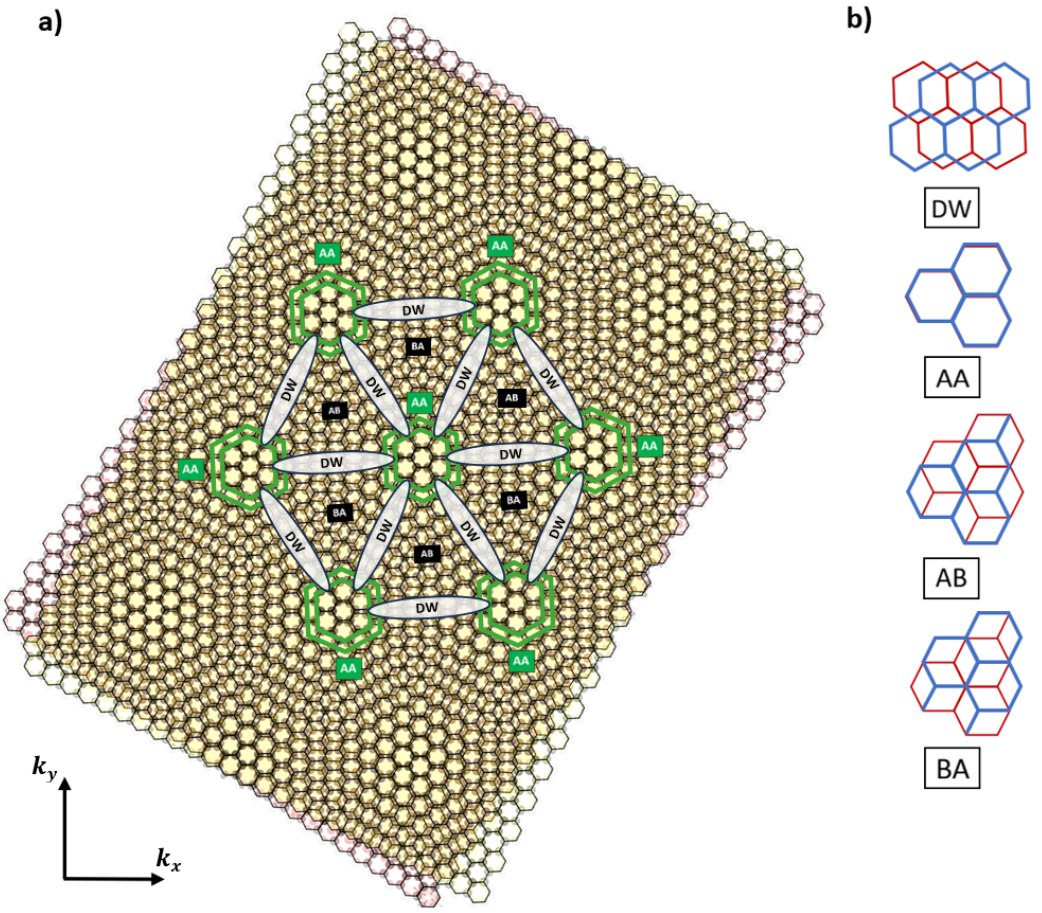

Figure 3.4: Moiré superlattice for twisted bilayer graphene, detailing the AA, AB/BA and DW stackings, (a) without atomic relaxation, (b) with atomic relaxation [47]. The Moiré pattern was made in Wolfram Mathematica.

alistic systems, the atomic positions are spontaneously adjusted to minimize the total energy, leading to local relaxation of the lattice.

This structural relaxation results in well-defined stacking domains. When the sublattice vertices of the upper layer are situated directly above those of the lower layer, the arrangement is known as AB stacking; if the configuration is reversed, it is known as BA stacking. Regions where the two layers are perfectly aligned (with atoms on the same sublattice vertically above each other) are termed AA stacking, which act as the nodes of the Moiré superlattice. The boundaries between AA regions, which separate the AB and BA domains, are called domain walls (DWs), as depicted in Fig. 3.4.

These stacking arrangements are energetically distinct: AA regions experience significant repulsion due to direct atomic overlap and therefore tend to contract, while the AB and BA domains expand, benefiting from a lower energy configuration. Domain walls naturally arise at the interfaces of these domains as a result of this relaxation process. Without such atomic relaxation,

the distinction and size of AA, AB and DW regions would be ill-defined or absent, limited to scales comparable to a single unit cell rather than the larger Moiré pattern.

To describe the electronic structure at this scale, we use the $(2+2)$-band model proposed by Bennett et. al. [21]. In this formalism, the total Hamiltonian is partitioned as follows

$$\mathcal{H}_k^{(2+2)} = \begin{pmatrix} \mathcal{H}_k^{*} & \mathcal{H}_k^{int} \\ \mathcal{H}_k^{int,\dagger} & \mathcal{H}_k^{\Delta} \end{pmatrix}, \tag{3-29}$$

where $\mathcal{H}_k^{*}$ is a 2×2 sub-matrix related to AA regions, modeled by a honeycomb lattice, $\mathcal{H}_k^{\Delta}$ is for the symmetric states localized along the domain walls, which serve as conduits connecting the AA sites, which also form a honeycomb lattice. The off-diagonal blocks encode couplings between two AA stackings, whereas the DW states provide additional bands at higher energies (typically above 10 meV, resembling auxiliary or complementary bands). The dominant hopping processes in AA regions are relatively weak (of the order of 10 meV), whereas those connecting DW regions are much stronger (around 1 eV).

To be more explicit, each block $\mathcal{H}_k^I$ (with $I = *, \Delta$, int) is represented following the conventions of Ref. [21], can be generally written as

$$\mathcal{H}_k^I = \begin{pmatrix} t_0^I + t_2^I f_2 & t_1^I f_1 + t_3^I f_3 \\ t_1^I f_1^\dagger + t_3^I f_3^\dagger & t_0^I + t_2^I f_2 \end{pmatrix} = \begin{pmatrix} d_0^I & d_-^I \\ d_+^I & d_0^I \end{pmatrix}, \tag{3-30}$$

where the real hopping parameters $\{t_0^I, t_1^I, t_2^I, t_3^I\}$ are specified for each subsystem, except t_3^{int}, which can generally be complex and encodes third nearest-neighbor interactions. The functions f_1, f_2, f_3 are defined as

$$\begin{aligned} f_1 &= \sum_{j=1}^{3} e^{i\boldsymbol{k}\cdot\boldsymbol{b}_j/\hbar}, \quad f_2 = \sum_{j=1}^{3} \cos(\boldsymbol{k}\cdot\boldsymbol{a}_j/\hbar) \\ f_3 &= \sum_{j=1}^{3} e^{-2i\boldsymbol{k}\cdot\boldsymbol{b}_j/\hbar}. \end{aligned} \tag{3-31}$$

These terms describe first, second, and third nearest-neighbor hoppings, respectively, on the honeycomb lattice.

3.2.2.1 Minimal two-band model

As the focus here is on the low-energy physics of TBG, we can simplify the original four-component spinor $\Phi = (\phi, \phi')$ by considering each as a two-component object. This allows us to write the eigenvalue problem for the Hamiltonian as follows

$$\mathcal{H}_k^{(2+2)}\Phi = E\Phi \Longrightarrow \begin{pmatrix} \mathcal{H}_k^{*} & \mathcal{H}_k^{int} \\ \mathcal{H}_k^{int,\dagger} & \mathcal{H}_k^{\Delta} \end{pmatrix} \begin{pmatrix} \phi \\ \phi' \end{pmatrix} = E \begin{pmatrix} \phi \\ \phi' \end{pmatrix}, \tag{3-32}$$

being ϕ the low-energy states, and ϕ' the highly dispersive states, to a effective energy-dependent Hamiltonian equation for ϕ in terms of $\mathcal{H}_k^{*}$, $\mathcal{H}_k^{\Delta}$ and $\mathcal{H}_k^{int}$

$$\mathcal{H}_k^{eff}\phi = E\phi. \tag{3-33}$$

So, we define an effective Hamiltonian

$$\mathcal{H}_k^{eff} = \mathcal{H}_k^{*} - \mathcal{H}_k^{int}(\mathcal{H}_k^{\Delta})^{-1}\mathcal{H}_k^{int\dagger} = \begin{pmatrix} d_0 & d_- \\ d_+ & d_0 \end{pmatrix}. \tag{3-34}$$

Moreover, since both $\mathcal{H}^I$'s and $\mathcal{H}^{eff}$ are 2×2 matrices, it is convenient to express them in terms of the identity matrix σ_0 and Pauli matrices $\sigma_\pm = \sigma_1 \pm i\sigma_2$. All the dependence on momentum $\boldsymbol{k}$ is incorporated into the coefficients $(d_0^I, d_1^I, d_2^I) \leftrightarrow (d_0^I, d_\pm^I = d_1^I \pm i d_2^I)$, which are defined as follows for any block I

$$\begin{aligned}
d_0^I &= t_0^I + t_2^I \sum_{j=1}^{3} \cos(\boldsymbol{k}\cdot\boldsymbol{a}_j/\hbar) \\
d_1^I &= t_1^I \sum_{j=1}^{3} \cos(\boldsymbol{k}\cdot\boldsymbol{b}_j/\hbar) + \mathrm{Re}t_3^I \sum_{j=1}^{3} \cos(2\boldsymbol{k}\cdot\boldsymbol{b}_j/\hbar) + \mathrm{Im}t_3^I \sum_{j=1}^{3} \sin(2\boldsymbol{k}\cdot\boldsymbol{b}_j/\hbar) \\
d_2^I &= -t_1^I \sum_{j=1}^{3} \sin(\boldsymbol{k}\cdot\boldsymbol{b}_j/\hbar) + \mathrm{Re}t_3^I \sum_{j=1}^{3} \sin(2\boldsymbol{k}\cdot\boldsymbol{b}_j/\hbar) - \mathrm{Im}t_3^I \sum_{j=1}^{3} \cos(2\boldsymbol{k}\cdot\boldsymbol{b}_j/\hbar),
\end{aligned} \tag{3-35}$$

the coefficients for the effective Hamiltonian $\mathcal{H}_k^{eff}$ are then given by

$$\begin{aligned}
d_0 &= d_0^{*} - \frac{1}{d_\Delta^2}\left[d_0^{int}d_0^{\Delta}d_0^{int} - d_-^{int}d_+^{\Delta}d_0^{int} - d_0^{int}d_-^{\Delta}d_+^{int} + d_-^{int}d_0^{\Delta}d_+^{int}\right], \\
d_- &= d_1 - id_2 = (d_+)^\dagger \\
&= d_1^{*} - id_2^{*} - \frac{1}{d_\Delta^2}\left[2d_0^{int}d_0^{\Delta}d_-^{int} - d_-^{int}d_+^{\Delta}d_-^{int} - d_0^{int}d_-^{\Delta}d_0^{int}\right],
\end{aligned} \tag{3-36}$$

where $d_\Delta^2 = (d_0^{\Delta})^2 - (d_1^{\Delta})^2 - (d_2^{\Delta})^2$. Although the diagonal component d_0 of $\mathcal{H}_k^{eff}$ influences the band energies, such that the eigenvalues are

$$\varepsilon_n = d_0 - d, \;\; \varepsilon_m = d_0 + d, \;\; d = \sqrt{d_1^2 + d_2^2}, \tag{3-37}$$

it does not appear in the eigenstates associated with the valence and conduction bands $|n\rangle$ and $|m\rangle$, which are given by

$$|n\rangle = \frac{1}{\sqrt{2}d}\begin{pmatrix} -d \\ d_1 + id_2 \end{pmatrix}, \;\; |m\rangle = \frac{1}{\sqrt{2}d}\begin{pmatrix} d \\ d_1 + id_2 \end{pmatrix}. \tag{3-38}$$

In the case where the effective model Hamiltonian takes the Dirac form $\mathcal{H}_k^{eff} = \sum_{i=0}^{2} d_i \sigma_i$ the quantum metric defined from the lower band eigenstate $|n\rangle$ is according to eq. (3-23) and (2-27) given by

$$\begin{aligned} g_{\mu\nu} &= \frac{1}{4d^2}\{\partial_\mu d_1 \partial_\nu d_1 + \partial_\mu d_2 \partial_\nu d_2 - \partial_\mu d \partial_\nu d\}, \\ &= \frac{1}{8d^2}\{\partial_\mu d_+ \partial_\nu d_- + \partial_\mu d_- \partial_\nu d_+ - 2\partial_\mu d \partial_\nu d\}. \end{aligned} \tag{3-39}$$

Here, $N = 2$ reflects the presence of two spin components. Since spin degeneracy has not been included in the previous calculation, the physically relevant quantum metric must be multiplied by a factor of two

$$g_{\mu\nu} \to g_{\mu\nu} \times 2, \tag{3-40}$$

this same factor applies to the fidelity number spectral function and the opacity, ensuring consistency with physical observables.

These bands are related to virtual $\boldsymbol{K}$ and $\boldsymbol{K}'$ points where are located the AA stackings (we say "virtual" because these stackings are minimized regions, no physical points), which were already defined previously. This redefinition of the AA stackings helps us to relate the similar behavior of the eigenstates obtained in eq. (3-38) to the case that appears in pristine graphene [2], it means the emergence of nodal points−i.e., energy band degeneracies−at the $\boldsymbol{K}$ and $\boldsymbol{K}'$ positions in the TBG structure. This is also evident in Fig. 3.5. Although our numerical calculations reveal a very small gap ($\Delta = 0.045$ meV) at these points, as displayed in Fig. 3.6, this gap is negligible in physical terms: It is several orders of magnitude smaller than the thermal energy at room temperature ($k_B T \sim 25$ meV), and thus does not materially affect our theoretical predictions.

In summary, these findings demonstrate that, provided that ISOC is absent, TBG maintains a semimetallic (Dirac-like) character closely analogous to monolayer graphene.

3.2.2.2 Quantum geometry and low frequency opacity of TBG

The band structure $\{\varepsilon_n, \varepsilon_m\}$, quantum metric $g_{\mu\nu}$, fidelity number spectral function $\mathcal{G}_{\mu\nu}(\omega)$, and opacity $\mathcal{O}_\mu(\omega)$ are computed numerically from the tight-binding model for TBG proposed by Bennett et al. [21]. Results for selected twist angles are presented in Fig. 3.5. Both $\mathcal{G}_{\mu\nu}(\omega)$ and $\mathcal{O}_{\mu\nu}(\omega)$ are obtained using the eq. (2-30), where the Dirac delta function representing optical transitions is approximated by a Lorentzian shape

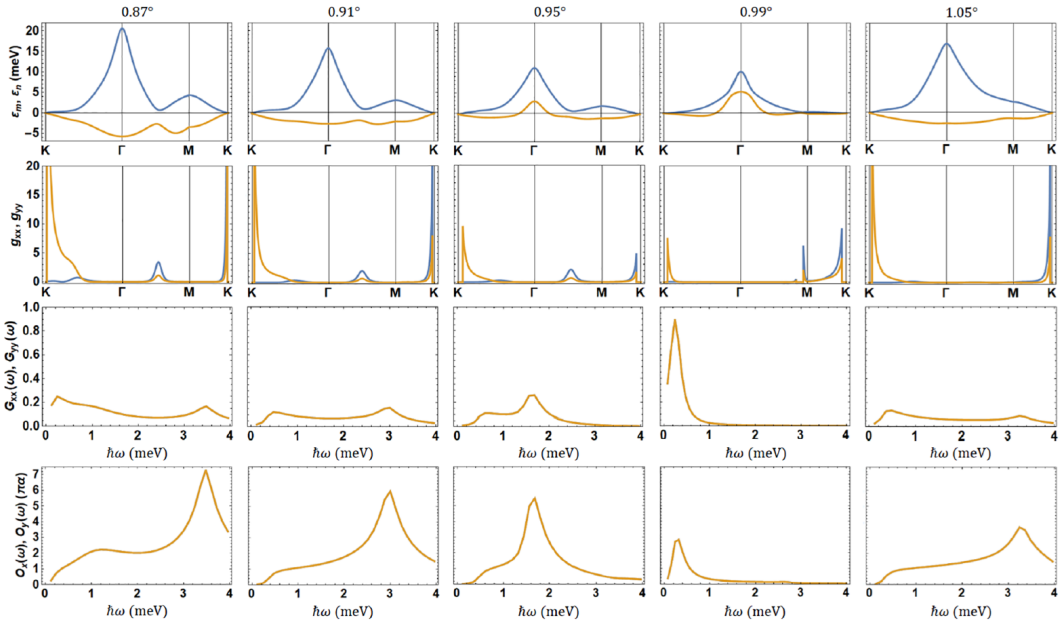

Figure 3.5: Numerical calculations for TBG at five distinct twist angles $\theta = 0.87^o$, 0.91^o, 0.95^o, 0.99^o, 1.05^o. From top to bottom, we show the electronic band structure $(\varepsilon_n, \varepsilon_m)$ and the quantum metric components (g_{xx}, g_{yy}) along high-symmetry lines in the BZ, followed by the fidelity-number spectral function $(\mathcal{G}_{xx}(\omega), \mathcal{G}_{yy}(\omega))$ and the absorbance for polarized light $(\mathcal{O}_x(\omega), \mathcal{O}_y(\omega))$,each displayed as a function of energy $\hbar\omega$.

$$\delta(\omega + \frac{\varepsilon_n}{\hbar} - \frac{\varepsilon_m}{\hbar}) \simeq \frac{\eta/\pi}{(\omega + \frac{\varepsilon_n}{\hbar} - \frac{\varepsilon_m}{\hbar})^2 + \eta^2}, \tag{3-41}$$

with $\eta = 0.1$ meV serving as a phenomenological broadening parameter to simulate correlation effects. Throughout this analysis, we restrict to zero temperature. The calculated band structure retains Dirac-like features at the $\boldsymbol{K}$ and $\boldsymbol{K}'$ points. Although the chemical potential is shifted to values between approximately 0.1 and 0.5 meV above the Dirac point, in agreement with the predictions of the Bennett model.

If the chemical potential μ were located precisely at the Dirac points, the quantum metric components g_{xx}, g_{yy} would diverge, and as a consequence, the low-frequency limit of the fidelity number spectral function $\{\mathcal{G}_{xx}(\omega), \mathcal{G}_{yy}(\omega)\}$ would display a $1/\omega$ divergence resulting in a constant, frequency-independent opacity at low frequencies [31].

However, due to the finite value of the chemical potential in our model, the region of nonzero quantum metric is confined away from the Dirac point, because only the region with only one band filled and one band empty can have nonzero quantum metric (this is the region where optical transition matrix element is the quantum metric). If both bands are filled ($\mu > 0$) or both bands

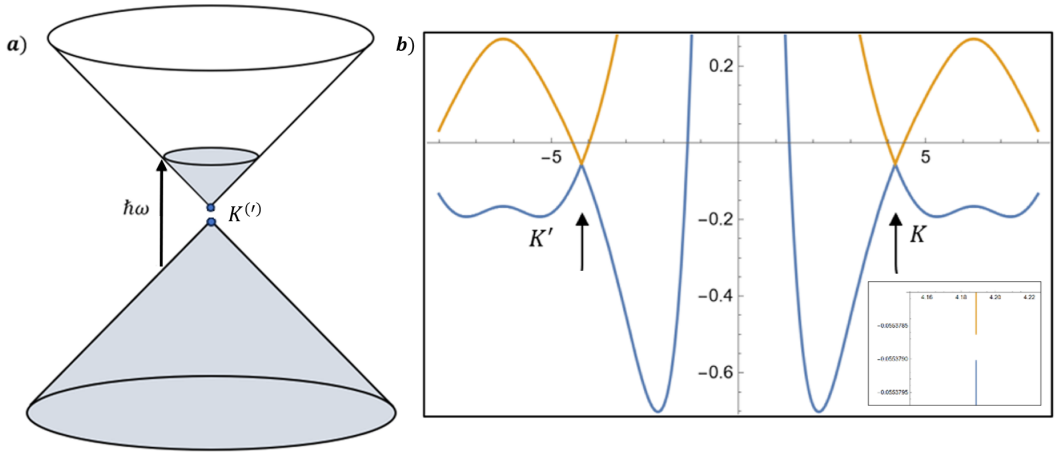

Figure 3.6: a) The effect of a finite chemical potential $\mu = 0.055$meV on the opacity of linear Dirac model. The figure shows schematically how the energy shift caused by the real part of self-energy blocks the optical transition in a low-frequency regime [31], b) Energy bands of TBG at $\theta = 0.99^o$ taking $k_y = 0$, we see the appearance of a nonzero gap $\Delta = 0.045$ μeV, that could be easily neglected in our model.

are empty ($\mu < 0$), the there is no optical transition and quantum metric is ill-defined.

Thus, the singular behavior at the $\boldsymbol{K}$ and $\boldsymbol{K}'$ points is eliminated, and $\{\mathcal{G}_{xx}(\omega), \mathcal{G}_{yy}(\omega)\}$ does not diverge as $\omega \to 0$. As a result, the opacity at zero frequency is suppressed, analogous to the behavior observed in fluorinated graphene when the chemical potential is displaced from the Dirac point [31,41], as depicted in Fig. 3.6.

A straightforward expectation is that TBG, consisting of two coupled graphene monolayers, should show an absorbance approximately twice that of a single sheet, given by

$$\overline{\mathcal{O}}(\omega) = \pi\alpha + (1 - \pi\alpha) \times \pi\alpha \approx 2\pi\alpha, \tag{3-42}$$

where this estimate is based on summing the optical absorption from each monolayer. This estimate of absorbance is valid primarily at frequencies exceeding the chemical potential, which is typically around $\hbar\omega \gtrsim 0.5$ meV, for most twist angles. However, for photon energies below $\hbar\omega \lesssim 0.5$ meV, the absorbance is notably reduced due to the influence of the finite chemical potential, as discussed above.

Furthermore, within the so-called magic range ($0.96^o \leq \theta \leq 1.02^o$), the model predicts especially flat valence and conduction bands that are almost identical in shape, but exhibit the following remarkable feature: In this regime (for example, as shown by the $\theta = 0.99^o$) result in Fig. 3.5, both the fidelity

number spectral function $\mathcal{G}_{xx}(\omega) \approx \mathcal{G}_{yy}(\omega)$ and the opacity $\mathcal{O}_{\mu}(\omega)$ display pronounced peaks at very low frequencies, around $\hbar\omega \approx 0.3$ meV. For higher frequencies, these quantities quickly diminish.

This behavior reflects the fact that, in a large region of the Brillouin zone, electrons can absorb photons of nearly the same energy (specifically, the energy corresponding to the separation between the two flat bands). The presence of a peak in $\mathcal{G}_{\mu\nu}(\omega)$ at $\hbar\omega \approx 0.3$ meV is a clear indication that the quantum metric is predominantly concentrated within the flat band region, particularly between the Γ and M points (see the band structure in Fig. 3.5 for $\theta = 0.99^{o}$).

These findings point to a close connection between an enhanced quantum metric and the formation of flat bands at the magic angle, providing support for the theoretical link between the quantum metric and the superfluid density [7–12].

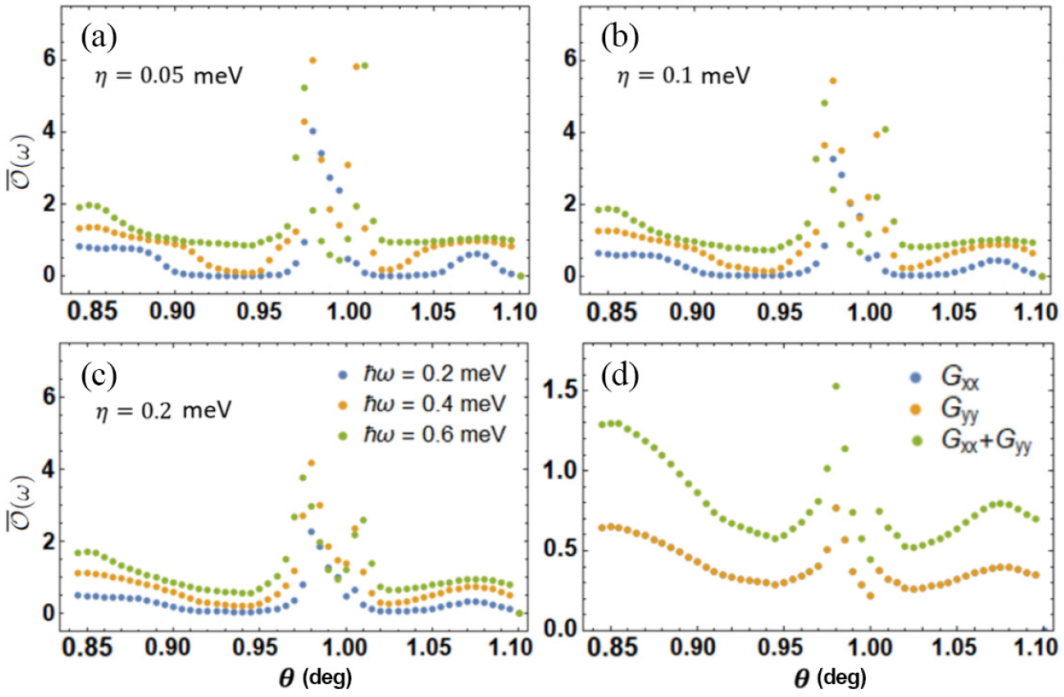

Figure 3.7: Opacity of TBG for unpolarized light $\tilde{\mathcal{O}}(\omega)$ at zero temperature, plotted as a function of twist angle θ for three selected frequencies $\hbar\omega = (0.2, 0.4, 0.6)$ meV. The results are presented for three distinct values of artificial broadening (a) $\eta = 0.05$ meV, (b) $\eta = 0.01$ meV, (c) $\eta = 0.2$ meV. These broadening parameters are phenomenological representations of different correlation strengths. (d) The fidelity number components $\{\mathcal{G}_{xx}, \mathcal{G}_{yy}, \mathcal{G}_{xx} + \mathcal{G}_{yy}\}$ are shown as functions of the twist angle θ.

From an experimental point of view, our quantum metric analysis suggests a straightforward test: If a substantial reduction in absorbance is detected

for $\hbar\omega \sim 0.1$ meV in the magic angle regime, or equivalently, if TBG becomes nearly transparent at millimeter wavelengths (as demonstrated by the simulations in Fig. 3.7 for varying values of the broadening parameter η), this would serve as indirect evidence for the presence of flat bands. By integrating the ratio of absorbance to frequency over ω (as in eq. (3-14)), one obtains the trace of the fidelity number, providing a measure of the total quantum metric associated with the flat bands. Using the effective tight-binding model, we computed this quantity as a function of the twist angle, as shown in Fig. 3.7(d), where both $\mathcal{G}_{xx}$ and $\mathcal{G}_{yy}$ reach their maximum near $\theta \approx 0.98^o$. It is important to note that the total fidelity number remains finite in this calculation only because the chemical potential eliminates the otherwise divergent quantum metric (i.e., the spread $\Omega_I = A_{cell}(\mathcal{G}_{xx} + \mathcal{G}_{yy})$), where A_{cell} is the area of the Moiré superlattice. In reality, this divergence would persist since the tight-binding model omits the ISOC at 55 μeV that would be required to regularize the spread. as discussed in Sec. 3.2.1 for monolayer graphene. Thus, the presence of a nonzero chemical potential in our model plays a crucial role in regularizing the quantum metric.

3.2.3 Transition metal dichalcogenides (TMDs)

3.2.3.1 Tight-binding model of TMDs

We now focus on monolayer hexagonal TMDs, of the form $1H - MX_2$, where the transition metal M is either Mo or W, and chalcogen X can be S, Se or Te. For our study, we employ the widely used tight-binding model described on Ref. [43]. This model emphasizes the role of the transition metal d orbitals closest to the energy gap, while minimizing the influence of s orbitals, and p orbitals are dominated by chalcogen atoms. As a result, this scheme is often referred to as the "three-band approximation".

In this approach, the basis set for the Hamiltonian consists of the d orbitals

$$|\psi_0\rangle = (d_{z^2}, d_{xy}, d_{x^2-y^2}), \tag{3-43}$$

and the corresponding hopping terms define a 3×3 tight-binding Hamiltonian

$$H_0(\boldsymbol{k}) = \begin{pmatrix} c_{k,1}^\dagger & c_{k,2}^\dagger & c_{k,3}^\dagger \end{pmatrix} \begin{pmatrix} V_0 & V_1 & V_2 \\ V_1^* & V_{11} & V_{12} \\ V_2^* & V_{12}^* & V_{22} \end{pmatrix} \begin{pmatrix} c_{k,1} \\ c_{k,2} \\ c_{k,3} \end{pmatrix}. \tag{3-44}$$

Here, $c_{k,I}^\dagger, c_{k,I}$ denote the creation and annihilation operators for each orbital,

and the various matrix elements are given explicitly as follows

$$
\begin{aligned}
V_0 &= \varepsilon_1 + 2t_0\Big(2\cos\alpha\cos\beta + \cos 2\alpha\Big) + 2r_0\Big(2\cos 3\alpha\cos\beta + \cos 2\beta\Big) \\
&\quad + 2u_0\Big(2\cos 2\alpha\cos 2\beta + \cos 4\alpha\Big)\,, \\
\mathrm{Re}[V_1] &= -2\sqrt{3}\,t_2\sin\alpha\sin\beta + 2(r_1+r_2)\sin 3\alpha\sin\beta - 2\sqrt{3}\,u_2\sin 2\alpha\sin 2\beta\,,
\end{aligned}
$$

$$
\begin{aligned}
\mathrm{Im}[V_1] &= 2t_1\sin\alpha\,(2\cos\alpha + \cos\beta) + 2(r_1-r_2)\sin 3\alpha\cos\beta \\
&\quad + 2u_1\sin 2\alpha\,(2\cos 2\alpha + \cos 2\beta)\,, \\
\mathrm{Re}[V_2] &= 2t_2\Big(\cos 2\alpha - \cos\alpha\cos\beta\Big) - \tfrac{2}{\sqrt{3}}(r_1+r_2)\Big(\cos 3\alpha\cos\beta - \cos 2\beta\Big) \\
&\quad + 2u_2\Big(\cos 4\alpha - \cos 2\alpha\cos 2\beta\Big)\,, \\
\mathrm{Im}[V_2] &= 2\sqrt{3}\,t_1\cos\alpha\sin\beta + \tfrac{2}{\sqrt{3}}\sin\beta\,(r_1-r_2)(\cos 3\alpha + 2\cos\beta) \\
&\quad + 2\sqrt{3}\,u_1\cos 2\alpha\sin 2\beta\,, \\
V_{11} &= \varepsilon_2 + (t_{11}+3t_{22})\cos\alpha\cos\beta + 2t_{11}\cos 2\alpha + 4r_{11}\cos 3\alpha\cos\beta \\
&\quad + 2\Big(r_{11} + \sqrt{3}\,r_{12}\Big)\cos 2\beta + (u_{11}+3u_{22})\cos 2\alpha\cos 2\beta + 2u_{11}\cos 4\alpha\,, \\
\mathrm{Re}[V_{12}] &= \sqrt{3}\,(t_{22}-t_{11})\sin\alpha\sin\beta + 4r_{12}\sin 3\alpha\sin\beta + \sqrt{3}\,(u_{22}-u_{11})\sin 2\alpha\sin 2\beta\,, \\
\mathrm{Im}[V_{12}] &= 4t_{12}\sin\alpha\,(\cos\alpha - \cos\beta) + 4u_{12}\sin 2\alpha\,(\cos 2\alpha - \cos 2\beta)\,, \\
V_{22} &= \varepsilon_2 + (3t_{11}+t_{22})\cos\alpha\cos\beta + 2t_{22}\cos 2\alpha + 2r_{11}\Big(2\cos 3\alpha\cos\beta + \cos 2\beta\Big) \\
&\quad + \tfrac{2}{\sqrt{3}}\,r_{12}\Big(4\cos 3\alpha\cos\beta - \cos 2\beta\Big) + (3u_{11}+u_{22})\cos 2\alpha\cos 2\beta + 2u_{22}\cos 4\alpha\,,
\end{aligned}
$$

where a is the lattice parameter of TMD material being used, $(\alpha,\beta) = (\frac{a}{2\hbar}k_x, \frac{\sqrt{3}a}{2\hbar}k_y)$, ε_j is the on-site energy corresponding to the atomic orbital $|\phi^j_\mu\rangle$, where j represents a category of symmetry in irreducible representation: $A_1'\{d_{z^2}\}$ for $j=1$, $E'\{d_{xy}, d_{x^2-y^2}\}$ for $j=2$, and μ is the label of the orbital in the category; then we denote the basis as $|\phi^1_1\rangle = d_{z^2}$, $|\phi^2_1\rangle = d_{xy}$ and $|\phi^2_2\rangle = d_{x^2-y^2}$ as is shown in Ref. [43]. And the other parameters $(t_0, t_1, t_2, t_{11}, t_{12}, t_{22}.r_0, r_1, r_2, r_{11}, r_{12}, u_0, u_1, u_2, u_{11}, u_{12}, u_{22})$ are parameters accurately determined by fitting the first principles (FP) energy bands of relaxed monolayers of MX_2 in generalized-gradient approximation (GGA). Is important to mention that, even the model is using a set of d orbitals of M, the parameters are fitted regarding p orbitals as an intermediate path ($d_a \rightarrow p_{ab} \rightarrow d_b$), so even the p orbitals are not used in the basis of the Hamiltonian, are too important in its construction.

For a more realistic case, we include the spin-orbit coupling (SOC), then the new basis consists of six-band model spanned by three transition metal d orbitals and their two spins projections

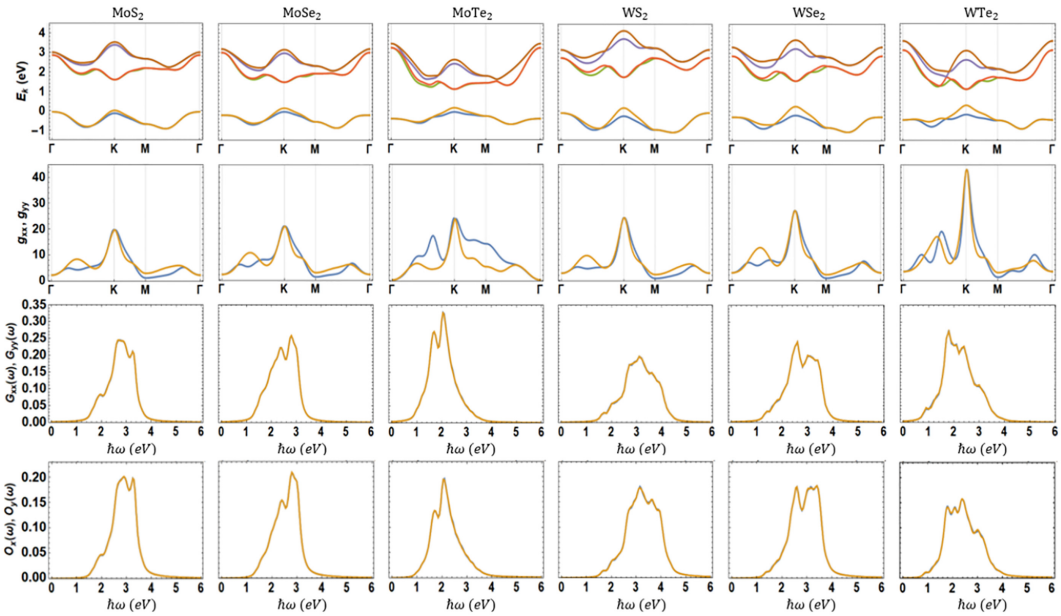

Figure 3.8: Model calculated band structure $(\varepsilon_n, \varepsilon_m)$ and quantum metric (g_{xx}, g_{yy}) displayed along the high-symmetry lines in the BZ, followed by fidelity-number spectral function $(\mathcal{G}_{xx}(\omega), \mathcal{G}_{yy}(\omega))$, and the absorbance $(\mathcal{O}_x(\omega), \mathcal{O}_y(\omega))$ under polarized light as functions of energy $\hbar\omega$ for the six TMD materials: MoS_2, $MoSe_2$, $MoTe_2$, WS_2, WSe_2 and WTe_2.

$$|\psi\rangle = (d_{z^2}\uparrow, d_{xy}\uparrow, d_{x^2-y^2}\uparrow, d_{z^2}\downarrow, d_{xy}\downarrow, d_{x^2-y^2}\downarrow), \tag{3-45}$$

and the full Hamiltonian 6×6 takes the form

$$H(\boldsymbol{k}) = I_2 \otimes H_0(\boldsymbol{k}) + H', \tag{3-46}$$

where $H' = \lambda \boldsymbol{L} \cdot \boldsymbol{S}$ is the SOC contribution to the Hamiltonian, being λ the strength of the SOC. It results

$$\begin{aligned} H(\boldsymbol{k}) &= \begin{pmatrix} H_0(\boldsymbol{k}) + \dfrac{\lambda}{2} L_z & 0 \\ 0 & H_0(\boldsymbol{k}) - \dfrac{\lambda}{2} L_z \end{pmatrix}, \\ L_z &= \begin{pmatrix} 0 & 0 & 0 \\ 0 & 0 & 2i \\ 0 & -2i & 0 \end{pmatrix}. \end{aligned} \tag{3-47}$$

Numerical calculations based on this model−including SOC−are presented in Fig. 3.8 for six different TMD materials. An artificial broadening parameter $\eta = 0.1$ eV is used in the simulation. These compounds display direct semiconducting gaps of roughly $1 - 2$ eV.

Their band structures comprise a single pair of spin-split valence bands and two pairs of spin-split conduction bands, placing their dominant optical

transitions across the infrared and visible ranges. Inspecting the quantum metric reveals peaks at the $\boldsymbol{K}$ and $\boldsymbol{K}'$ valleys, which, unlike pristine graphene, remains finite. As a result, both the TMD's fidelity numbers $\mathcal{G}_{\mu\nu}$ and the spreads of the WF Ω_I are finite too. Computing the spread through momentum-space integration (eq. (2-33)) or via the frequency integral (eq. (3-14)) yields the values of Ω_I summarized in Table 3.2.

Table 3.2: Area of the unit cell A_{cell}, spread of the valence-band WFs Ω_I, the dimensionless ratio $\Omega_I/A_{\text{cell}} = \text{Tr}\, G_{\mu\nu}$ and the band gap in the K point with and without SOC, calculated from the tight-binding model of Ref. [43].

Mat.	$\boldsymbol{A_{\text{cell}}}$ (Å^2)	$\boldsymbol{\Omega_I}$ (Å^2)	$\boldsymbol{\Omega_I/A_{\text{cell}} = \text{Tr}\, G_{\mu\nu}}$	$\boldsymbol{\Delta_K^S}$ (eV)	$\boldsymbol{\Delta_K}$ (eV)
MoS_2	26.44	16.95	0.641	1.585	1.658
WS_2	26.45	17.22	0.651	1.595	1.806
$MoSe_2$	28.74	19.57	0.681	1.338	1.429
WSe_2	28.72	20.36	0.709	1.313	1.541
$MoTe_2$	32.87	24.42	0.743	0.965	1.072
WTe_2	32.93	26.31	0.799	0.829	1.067

For these materials, the dimensionless ratio $\Omega_I/A_{cell} = \text{Tr}\mathcal{G}_{\mu\nu}$ lies between 0.6 and 0.8, indicating that their corresponding WFs are fairly localized compared to the unit cell area. Additionally, the absorbance $\overline{\mathcal{O}}(\omega)$ predicted by this model agrees closely with experimental measurements on free-standing TMD monolayers under unpolarized illumination at low photon energies ($\hbar\omega \lesssim 3$ eV) [42, 44, 45]. In summary, this minimal model−based only on the three transition metal d orbitals−provides an accurate description of both the essential low-energy optical response and the quantum geometric properties of these TMD systems.

3.2.3.2 Absorbance marker of TMDs with impurities

Building upon a method introduced by Bianco and Resta for calculating the Chern number [46, 49], we adopt a similar strategy to evaluate the optical conductivity to a lattice system in real space. Using the projector formalism, we note that

$$|\psi_{lk}\rangle\langle\psi_{lk}| = \int \frac{\mathrm{d}^2k}{\hbar^2 V_{BZ}} |\psi_{lk'}\rangle\langle\psi_{lk'}| = |E_{lk'}\rangle\langle E_{lk'}|, \tag{3-48}$$

where $\langle l|i\partial_\mu|l'\rangle = \langle\psi_{lk}|\hat{x}_\mu|\psi_{l'k}\rangle/\hbar$. Inserting these projectors into the formula for optical conductivity, we obtain

$$\sigma_{\mu\mu}(\omega) = \left(\frac{\pi e^2}{A_{cell}\hbar}\right)\omega\int\frac{\mathrm{d}^2k}{\hbar^2V_{BZ}}\int\frac{\mathrm{d}^2k'}{\hbar^2V_{BZ}}\sum_{l<l'}\langle\psi_{lk}|\hat{x}_\mu|\psi_{l'k'}\rangle\langle\psi_{l'k'}|\hat{x}_\mu|\psi_{lk}\rangle \times [f(\varepsilon_l^k) - f(\varepsilon_{l'}^k)]\delta(\omega + \frac{\varepsilon_l^k}{\hbar} - \frac{\varepsilon_{l'}^k}{\hbar}).$$

This expression can be simplified as

$$\sigma_{\mu\mu}(\omega) = \left(\frac{\pi e^2\omega}{A_{cell}\hbar}\right)\sum_{l<l'}\mathrm{Tr}\left[\hat{S}_l\hat{x}_\mu\hat{S}_{l'}\hat{x}_\mu\hat{S}_l\right][f(\varepsilon_l^k) - f(\varepsilon_{l'}^k)]\delta(\omega + \frac{\varepsilon_l^k}{\hbar} - \frac{\varepsilon_{l'}^k}{\hbar}), \quad (3\text{-}49)$$

where $\hat{S}_l = |E_l\rangle\langle E_l|$.

At this point, we can define a position-dependent version of the optical conductivity (also referred to as the **optical conductivity marker**), which reads

$$\sigma_{\mu\mu}(\boldsymbol{r},\omega) = \left(\frac{\pi e^2\omega}{A_{cell}\hbar}\right)\sum_s\langle\boldsymbol{r},s|\sum_{l<l'}\left[\hat{S}_l\hat{x}_\mu\hat{S}_{l'}\hat{x}_\mu\hat{S}_l\right]|\boldsymbol{r},s\rangle \times [f(\varepsilon_l^k) - f(\varepsilon_{l'}^k)]\delta(\omega + \frac{\varepsilon_l^k}{\hbar} - \frac{\varepsilon_{l'}^k}{\hbar}), \quad (3\text{-}50)$$

where the sum runs over all internal degrees of freedom s at site r. This formula provides a way to compute the optical response locally at any lattice position. For greater convenience, we introduce the operator

$$\mathcal{M}_\mu(\omega) = \sum_{l<l'}\hat{S}_l\hat{x}_\mu\hat{S}_{l'}\sqrt{(f(\varepsilon_l) - f(\varepsilon_{l'}))\delta\left(\omega + \frac{\varepsilon_l}{\hbar} - \frac{\varepsilon_{l'}}{\hbar}\right)}, \quad (3\text{-}51)$$

so that

$$\sigma_{\mu\mu}(\boldsymbol{r},\omega) = \left(\frac{\pi e^2\omega}{A_{cell}\hbar}\right)\sum_s\langle\boldsymbol{r},s|\mathcal{M}_\mu(\omega)\mathcal{M}_\mu^\dagger(\omega)|\boldsymbol{r},s\rangle. \quad (3\text{-}52)$$

Similarly, we can introduce the **absorbance marker** [35], that is, local absorption defined as

$$\overline{\mathcal{O}}(\boldsymbol{r},\omega) = \frac{2\pi^2\alpha}{A_{cell}}\omega\sum_s\sum_\mu\langle\boldsymbol{r},s|\mathcal{M}_\mu(\omega)\mathcal{M}_\mu^\dagger(\omega)|\boldsymbol{r},s\rangle, \quad (3\text{-}53)$$

that was averaged in μ directions. This framework can be used to define a local, gauge-invariant spread

$$\Omega_I(\boldsymbol{r}) = A_{cell}\int_0^\infty\mathrm{d}\omega\frac{1}{2\pi\omega}\left[\frac{\overline{\mathcal{O}}(\boldsymbol{r},\omega)}{\pi\alpha}\right] = A_{cell}\mathrm{Tr}\mathcal{G}_{\mu\nu}^d(\boldsymbol{r}), \quad (3\text{-}54)$$

where $\mathcal{G}_{\mu\nu}^d(\boldsymbol{r})$ defined as the **fidelity marker**, obtained from eqs. (2-31) and (3-52)

$$\mathcal{G}_{\mu\mu}^d(\boldsymbol{r},\omega) = \frac{1}{A_{cell}}\sum_s\mathrm{Re}[\langle\boldsymbol{r},s|\mathcal{M}_\mu(\omega)\mathcal{M}_\mu^\dagger(\omega)|\boldsymbol{r},s\rangle], \quad (3\text{-}55)$$

and integrating over frequency as shown in eq. (2-29).

To construct the states $|E_l\rangle$, we proceed by performing a Fourier transform from momentum to real space for the creation operators

$$c^\dagger_{k,I} = \sum_{i_1} e^{i\boldsymbol{k}\cdot\boldsymbol{r}_{i_1}} c^\dagger_{i_1,I}, \tag{3-56}$$

where $c^\dagger_{i_1,I}, c_{i_1,I}$ create and annihilate a particle in orbital I at site r_{i_1} .

With this transformation, each operator acts on three orbitals per site, extending the original 3×3 hamiltonian to $3L^2 \times 3L^2$ matrix if there are L atoms per lattice direction (i.e., $N = L^2$ sites). For instance, setting $L = 14$ leads to a system with $14 \times 14 = 196$ atoms, each with three orbitals, resulting in a total Hamiltonian of dimension $(3 \cdot 14^2) \times (3 \cdot 14^2)$.

The eigenvectors $|E_l\rangle$ contain 3×14^2 components, quite distinct from the eigenstates of $H_0(\boldsymbol{k})$ in momentum space (their eigenstates have only 3 elements). To enforce periodic boundary conditions (PBC), we use the **exponential position operator**

$$\hat{x} = \frac{L}{2\pi}\text{diag}\left(e^{2\pi i/L}, e^{4\pi i/L}, e^{6\pi i/L} \dots e^{2\pi i}\right) \otimes I_s, \tag{3-57}$$

where I_s is a $s \times s$ identity matrix, meaning that all three orbital degrees of freedom s inside the same unit cell share an identical position operator (now, we ignore the spin degrees of freedom, since the SOC is a very small energy scale compared to the optical transition range, so presumably it does not influence much in the absorbance spectrum). It is possible to appreciate that this operator adds complex elements to the definition of the markers. This is fixed by redefining them by taking the module

$$\begin{aligned} \sigma_{\mu\mu}(\boldsymbol{r},\omega) &\to \left[(\text{Re}\sigma_{\mu\mu}(\boldsymbol{r},\omega))^2 + (\text{Im}\sigma_{\mu\mu}(\boldsymbol{r},\omega))^2\right]^{1/2} \\ \mathcal{O}(\boldsymbol{r},\omega) &\to \left[(\text{Re}\mathcal{O}(\boldsymbol{r},\omega))^2 + (\text{Im}\mathcal{O}(\boldsymbol{r},\omega))^2\right]^{1/2}. \end{aligned} \tag{3-58}$$

With this change, we only care about the amplitude of the marker, being precisely what we can experimentally appreciate. Through this position operator, we produce the absorbance marker shown in Fig. 3.9.

In this case, the value found in the homogeneous limit is $\Omega_I = 13.557\mathring{A}^2$, which differs from our last result shown in Table 3.2 in 21.272%. It is a large difference, but is understandable due to the finite size effect in our numerical computation (since a 14×14 lattice requires significant computational time, which is why we do not include the SOC contribution here). The presence of a single impurity is represented as a Hamiltonian $H^{U_{imp}}_{3N\times 3N}$ with all elements equal to zero, but the diagonal, where the potential of the impurity is repeated in its 3 degrees of freedom. Thus, setting $U_{imp} = 0.5$, 1.5 and 3.0 eV, we put this number in the 3 positions of $H^{U_{imp}}$ that represent the position analyzed,

and all the others are zero.

We can appreciate a small difference between the absorbance marker in the central location and the absorbance measured in $k-$space. However, there are significant differences in the presence of impurities, and this will be mentioned here.

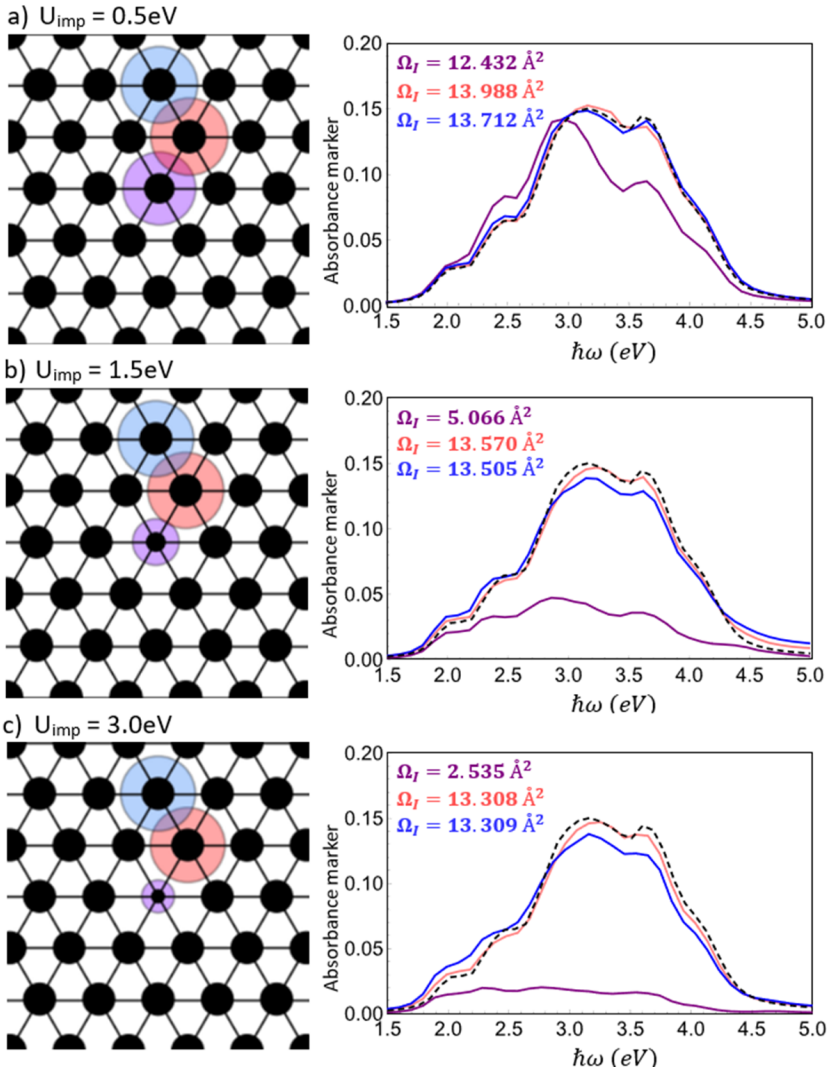

Figure 3.9: Comparison of density of particles (black circles) and spreads of WFs measured with the absorbance marker in the position of the single impurity (purple), next-neighbor (red) and next-next-neighbor (blue) in a 14×14 lattice using $\eta = 0.1$, in the WS_2, where: a) $U_{imp} = 0.5$ eV, b) $U_{imp} = 1.5$ eV and c) $U_{imp} = 3.0$ eV. The black dashed line is related to the clean case, where $\Omega_I = 13.557$ Å^2 and the density of particles is equal to 1 in any position. It can be observed how the spread noticeably decreases its extension due to the presence of the positive impurity. There are also very local decreasing in the density of particles in every case.

This phenomena is easier to be explained within the context of the absorbance marker. The absorbance with a single impurity with positive

potential is drastically decreased, which tells us that a single impurity with positive potential makes it difficult for the material to absorb light as a clean sample normally would. Intuitively, this is because the positive impurity potential repels electrons on the impurity site, so there are less electrons occupying the filled valence band states, and hence the spread of valence band WFs is reduced. Alternatively, one can also interpret it as there are less valence electrons available to absorb light on the impurity site, so the absorbance is reduced.

We now proceed to consider the many-impurity case that is more relevant to the experimental realization of disordered TMD materials in the macroscopic scale. We aim to describe the experimentally measured absorbance in the macroscopic scale disordered TMD that contains some densities of impurities.

To do this, we use the empirical relation

$$\mathcal{O}_{MI}(\omega) = (n_{imp})\mathcal{O}_{1-imp}(\omega) + (1 - n_{imp})\mathcal{O}_{H}(\omega), \tag{3-59}$$

where $\mathcal{O}_{MI}(\omega)$ is the absorbance with many impurities in the macroscopic scale, $\mathcal{O}_{1-imp}(\omega)$ is the absorbance marker on the impurity site, and $\mathcal{O}_{H}(\omega)$ is the absorbance in the homogeneous sample (clean case), and n_{imp} is the density of impurities on the sample. Both $\mathcal{O}_{1-imp}(\omega)$ and $\mathcal{O}_{H}(\omega)$ are shown in Fig. 3.9. This empirical formula is based on the single-impurity result presented in the previous section, which shows that the absorbance is suppressed very locally on the impurity site. As a result, when many impurities are present and the impurity density is low, we assume that each impurity suppresses the absorbance in its neighborhood, so the suppression of absorbance in the macroscopic scale should be proportional to the impurity density.

Our marker formalism suggests a straightforward experimental route: record the macroscopic absorbance, which equals the spatial average of local quantities

$$\{\overline{\Omega_I}, \overline{\mathrm{Tr}\mathcal{G}^d_{\mu\nu}}, \overline{\mathcal{O}(\omega)}\} = \frac{1}{N}\sum_{\boldsymbol{r}}\{\Omega_I(\boldsymbol{r}), \mathrm{Tr}\mathcal{G}^d_{\mu\nu}, \mathcal{O}(\boldsymbol{r},\omega)\}. \tag{3-60}$$

Hence, the protocol of eq. (3-12)−divide the bulk absorbance $\overline{\mathcal{O}(\omega)}$ by ω and the integrate over frequency−yields the spatially averaged fidelity marker $\overline{\mathrm{Tr}\mathcal{G}^d_{\mu\nu}} = \overline{\Omega_I}/A_{cell}$. These quantities can be readily measured, providing a concrete way to quantify the quantum quantum geometry of a disordered sample.

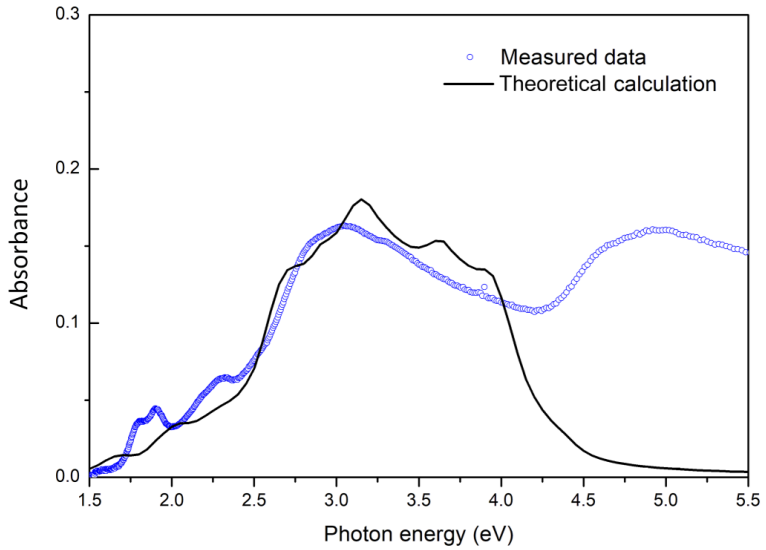

Figure 3.10: Absorbance of WS_2 measured at room temperature on a fused silica (blue circles) and theoretical calculation at zero temperature (black line) based on three-orbital model.

3.2.3.3 Absorbance of WS_2 on fused silica: Comparison between clean and disordered cases

We present the experimental results and some considerations are addressed with respect to the extraction of the gauge-invariant spread Ω_I from the room-temperature absorbance data of WS_2 placed on fused silica substrates. Particularly, aspects related to the involvement of higher-energy electronic bands and excitonic effects are discussed.

In Fig. 3.10 we display the data obtained from Ref. [50] as blue circles, and is compared with the SOC case shown in Fig. 3.8 by a black curve obtained through the $k-$integration for a clean WS_2. Now, we analyze the main differences.

The experimental data agree very well with the theoretical calculation for photon energies $\hbar\omega \lesssim 4$ eV, meaning that the tight-binding model employing only three d orbitals of W captures the absorbance in the low frequency range very accurately. At higher frequencies $\hbar\omega \gtrsim 4$ eV, the calculated absorbance falls to zero whereas the measured one remains finite. These additional values arise from optical transitions that involve p orbitals of S, and contribute to the spread of valence-band Wannier orbitals. As chalcogen orbitals are not included in the minimal tight-binding model of Ref. [43], a more elaborate tight-binding description or first-principle calculations would be needed to capture this part of the spectrum.

A further complication that cannot be avoided experimentally is the formation of excitons: two peaks around 1.9 and 2.3 eV. These excitons

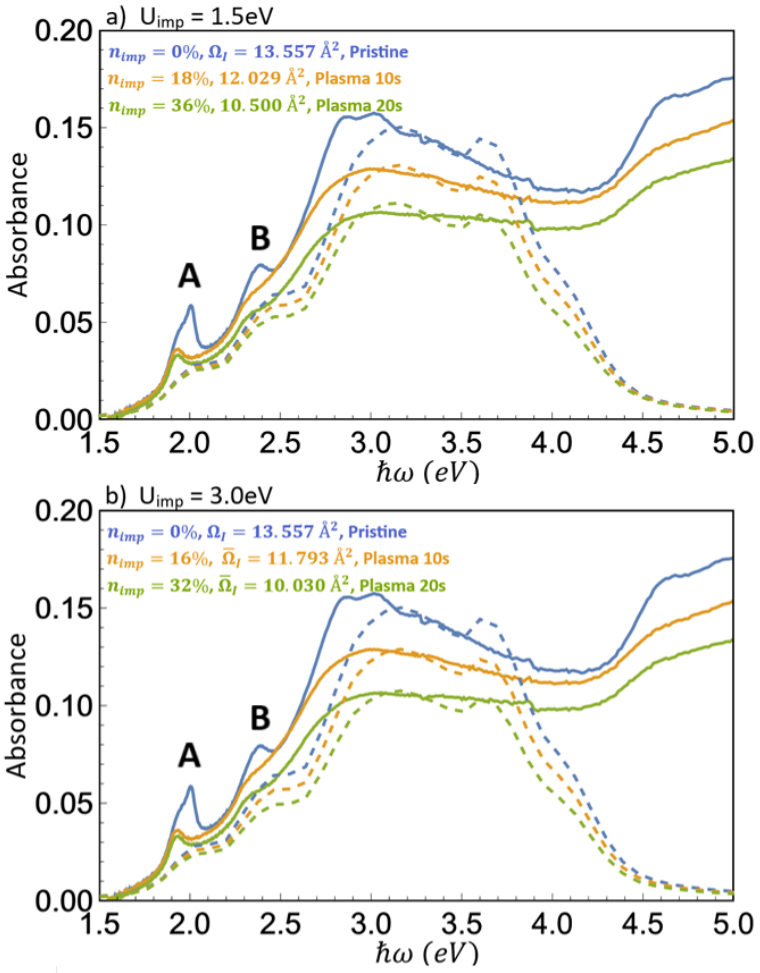

Figure 3.11: Absorbance of WS_2 measured at room temperature on a fused silica, with impurities induced by plasma in different exposure times (solid lines) [51], and theoretical calculations fitting the empirical formula with different densities and impurity potentials a) $U_{imp} = 1.5$ eV, and b) $U_{imp} = 3.0$ eV (dashed lines).

do not contribute to the spread Ω_I since excitons are bosons (we build the optical conductivity using Fermi distributions) and only appear after a photoexcitation process, their presence does not describe the ground state of the system, so we ignore these peaks in this discussion. Then, we conclude that we may extract the spread Ω_I from experimental absorbance data $\overline{\mathcal{O}}(\omega)$ using equation (3-14), provided that exciton absorption peaks are not taken into account.

Applying the equation (3-60) for macroscopic scale absorbance measured in disordered 2D semiconductors, we analyze the experimental absorbance data of Ref. [51]. In that work, monolayers WS_2 films deposited on fused silica substrates are treated with plasma, and their density of impurities can be controlled by the exposure time. After each plasma exposure, the absorbance of the WS_2 sample was re-measured, giving the cumulative results for 10 and 20 seconds, which are presented in Fig. 3.11. That absorption spectrum exhibits

pronounced excitonic resonances at approximately 1.9 eV (A exciton) and 2.3 eV (B exciton), just like in the clean WS_2 presented in Fig. 3.10 above. For pristine WS_2, the interband absorbance rises gradually from the gap edge ∼1.5 eV to the maximum near ∼3.0 eV−this region of the spectrum is almost entirely dominated by transitions involving the three d orbitals of W−that can be well-described by our theoretical model in Sec. 3.2.3. Above $\gtrsim$ 4.0 eV, the bands derived from the S atoms begin to contribute, moving beyond the scope of the minimal three-orbital description.

Fig. 3.11 shows that plasma treatment systematically reduces the absorbance, with greater suppression for longer exposure. This trend is attributed to preferential S atoms removal: sulfur vacancies deplete charge carriers around those sites and reduce interband transitions, as argued above. Because the tight-binding Hamiltonian includes only W orbitals, we mimic the resulting electron depletion by adding a positive potential U_{imp} on selected W sited, which was exactly described in the Sec. 3.2.3.2.

Figure 3.9 showed that such a local potential strongly decreases the absorbance in its immediate vicinity; therefore, a sample with randomly distributed vacancies can be modeled by the spatially averaged spread, fidelity marker and absorbance of the plasma-treated sample in the macroscopic scale defined in eq. (3-62) by the empirical formula

$$\begin{aligned} \overline{A} &= (n_{imp})A_{1-imp} + (1 - n_{imp})A_H \\ A &= \{\Omega_I, \mathrm{Tr}\mathcal{G}^d_{\mu\nu}, \mathcal{O}(\omega)\}, \end{aligned} \tag{3-61}$$

where A_{1-imp} is the local marker on the impurity site, A_H is the value in the homogeneous sample. This empirical formula presumes that each defect suppresses absorbance only locally−a notion supported by Fig. 3.9−so the macroscopic reduction should scale with n_{imp}.

Fitting the measured spectra using equation (3-61) can be achieved with either a moderated impurity potential and higher density of impurities (e.g. U_{imp} = 1.5 eV and n_{imp} = 18% generated per 10 seconds of exposure) or, equivalently, a larger impurity potential and lower density (e.g. U_{imp} = 3.0 eV and n_{imp} = 16% per 10 seconds). A definitive determination of U_{imp} under plasma conditions would require ab-initio kinetic simulations, which lie beyond our present scope. Nonetheless, the close agreement between the experimental absorbance in Fig. 3.11 and the empirical prediction of equation (3-59) demonstrates that−even within a simple tight-binding framework with only d orbitals of W atoms− our absorbance marker successfully captures both the local response near impurity sites and the experimentally measured absorbance in the macroscopic limit.

4
Conclusions

In conclusion, by leveraging the quantum metric perspective, we propose an optical absorption-based method to determine the gauge-invariant component of the spread (Ω_I) of occupied valence band Wannier functions. It represents a fundamental ground-state property characteristic of semiconductors and insulators. Our theoretical framework stems from recognizing that the spread of the valence band Wannier functions has a quantum-geometric origin, with the quantum metric of these states formally coinciding with optical transition matrix elements. For three-dimensional systems, we show that the spread of WFs can be extracted directly by integrating the imaginary part of the dielectric function over frequency and then multiplying it by the unit cell volume. This resulting quantity corresponds to an average measure of distances within the Brillouin zone when the latter is endowed with a curved (non-trivial) quantum metric, a measure we term the fidelity number. Using published experimental data on the dielectric function of silicon (Si), germanium (Ge), and bismuth telluride (Bi_2Te_3), we successfully determined the absolute magnitude of Ω_I. Furthermore, we interpret the dimensionless ratio $\Omega^{3/2} I/V_{cell}$ as an effective measure to characterize insulating properties, underlining the broad applicability of our methodology.

For two-dimensional systems, we suggest measuring the spread of WFs normalized by the unit cell area (Ω_I/A_{cell}) through the frequency-integrated optical absorbance divided by frequency. The application of this approach to graphene highlights the critical role of intrinsic spin-orbit coupling (ISOC) in obtaining a finite spread of WFs, which solves the divergence issue of the quantum metric at Dirac points. Additionally, measurement of the microwave range absorbance of graphene in the sub-Kelvin regime can directly quantify the magnitude of ISOC. We further investigate a recently introduced tight-binding model for structurally-relaxed twisted bilayer graphene (TBG), exploring its quantum geometric properties and optical absorption across various twist angles. Our analysis, focused on frequencies $\hbar\omega \lesssim 0.1$ meV, provides a practical means to detect the emergence of quasi-flat bands and map the associated quantum metric, potentially offering experimental evidence linking unconventional superconductivity in TBG to its quantum geometry.

Applying our approach to hexagonal transition metal dichalcogenides (TMDs) produces absorbance predictions that are in excellent agreement with the experimental data. We estimate that the ratio Ω_I/A_{cell} from the metal orbitals (Mo, W), typically ranges from approximately 0.6 to 0.8. Lastly, we employed the same parameters to construct a real-space Hamiltonian on a 14×14 lattice to investigate WS_2 samples containing single impurities characterized by impurity potentials $U_{imp} = 1.5$ eV and 3.0 eV. Our analysis clearly shows how these impurities alter both the intensity and frequency range of optical absorption. Furthermore, we successfully modeled the experimentally observed decrease in average absorbance as a function of the impurity density n_{imp} and the potential U_{imp}, demonstrating the robustness and precision of our approach. These results could help us conduct experiments where improved light absorption is needed for higher frequencies.

In summary, our proposed experimental protocol to extract Ω_I is robust and versatile, applicable to free-standing or substrate-supported two-dimensional materials, irrespective of their chemical composition or practical experimental complexities.

Bibliography

[1] PROVOST, J. P.; VALLEE, G.. **Riemannian structure on manifolds of quantum states.** Commun. Math. Phys., 76:289, 1980.

[2] VON GERSDORFF, G.; CHEN, W.. **Measurement of topological order based on metric-curvature correspondence**. Phys. Rev. B, 104:195133, Nov 2021.

[3] MERA, B.; ZHANG, A. ; GOLDMAN, N.. **Relating the topology of dirac hamiltonians to quantum geometry: When the quantum metric dictates chern numbers and winding numbers**. SciPost Phys., 12:018, 2022.

[4] KOMISSAROV, I., H. T. . Q. R.. **The quantum geometric origin of capacitance in insulators**. Nat Commun, 15:4621, May 2024.

[5] CHEN, W.; GERSDORFF, G. V.. **Measurement of interaction-dressed berry curvature and quantum metric in solids by optical absorption**. SciPost Phys. Core, 5:040, 2022.

[6] PORLLES, D.; CHEN, W.. **Quantum geometry of singlet superconductors**. Phys. Rev. B, 108:094508, Sep 2023.

[7] TÖRMÄ, S. P. . P.. **Superfluidity in topologically nontrivial flat bands**. Nat Commun, 6:094508, Nov 2015.

[8] JULKU, A.; PEOTTA, S.; VANHALA, T. I.; KIM, D.-H. ; TÖRMÄ, P.. **Geometric origin of superfluidity in the lieb-lattice flat band**. Phys. Rev. Lett., 117:045303, Jul 2016.

[9] LIANG, L.; VANHALA, T. I.; PEOTTA, S.; SIRO, T.; HARJU, A. ; TÖRMÄ, P.. **Band geometry, berry curvature, and superfluid weight**. Phys. Rev. B, 95:024515, Jan 2017.

[10] HERZOG-ARBEITMAN, J.; PERI, V.; SCHINDLER, F.; HUBER, S. D. ; BERNEVIG, B. A.. **Superfluid weight bounds from symmetry and quantum geometry in flat bands**. Phys. Rev. Lett., 128:087002, Feb 2022.

[11] PEOTTA, SEBASTIANO, B. B. A.. **Superconductivity, superfluidity and quantum geometry in twisted multilayer systems**. Nature Reviews Physics, 4:528–542, Aug 2022.

[12] ISKIN, M.. **Extracting quantum-geometric effects from ginzburg-landau theory in a multiband hubbard model**. Phys. Rev. B, 107:224505, Jun 2023.

[13] MARZARI, N.; VANDERBILT, D.. **Maximally localized generalized wannier functions for composite energy bands**. Phys. Rev. B, 56:12847–12865, Nov 1997.

[14] MARZARI, N.; MOSTOFI, A. A.; YATES, J. R.; SOUZA, I. ; VANDERBILT, D.. **Maximally localized wannier functions: Theory and applications**. Rev. Mod. Phys., 84:1419–1475, Oct 2012.

[15] BLOUNT, E. I.. **Formalisms of band theory**. Journal of Physics C: Solid State Physics, 13:305–373, 1962.

[16] ASHCROFT, N. W.; MERMIN, N. D.. **Solid state physics**. Saunders College Publishing, New York, NY, 1976.

[17] MANDELUNG, O.. **Semiconductors: Data Handbook**. Springer, Berlin, 2004.

[18] REED, B. W.; CHEN, J. M.; MACDONALD, N. C.; SILCOX, J. ; BERTSCH, G. F.. **Fabrication and stem/eels measurements of nanometer-scale silicon tips and filaments**. Phys. Rev. B, 60:5641–5652, Aug 1999.

[19] GREENAWAY, D.; HARBEKE, G.. **Band structure of bismuth telluride, bismuth selenide and their respective alloys**. Journal of Physics and Chemistry of Solids, 26(10):1585–1604, 1965.

[20] KOCHAN, D.; IRMER, S. ; FABIAN, J.. **Model spin-orbit coupling hamiltonians for graphene systems**. Phys. Rev. B, 95:165415, Apr 2017.

[21] BENNETT, D.; LARSON, D. T.; SHARMA, L.; CARR, S. ; KAXIRAS, E.. **Twisted bilayer graphene revisited: Minimal two-band model for low-energy bands**. Phys. Rev. B, 109:155422, Apr 2024.

[22] MATSUURA, S.; RYU, S.. **Momentum space metric, nonlocal operator, and topological insulators**. Phys. Rev. B, 82:245113, Dec 2010.

[23] SOUZA, I.; VANDERBILT, D.. **Dichroic f-sum rule and the orbital magnetization of crystals**. Phys. Rev. B, 77:054438, Feb 2008.

[24] DE SOUSA, M. S. M.; CRUZ, A. L. ; CHEN, W.. **Mapping quantum geometry and quantum phase transitions to real space by a fidelity marker**. Phys. Rev. B, 107:205133, May 2023.

[25] MAHAN, G. D.. **Many-Particle Physics**. Springer, New York, 2000.

[26] SOUZA, I.; WILKENS, T. ; MARTIN, R. M.. **Polarization and localization in insulators: Generating function approach**. Phys. Rev. B, 62:1666–1683, Jul 2000.

[27] RESTA, R.. **Why are insulators insulating and metals conducting?** Journal of Physics: Condensed Matter, 14(20):R625, may 2002.

[28] RESTA, R.. **The insulating state of matter: a geometrical theory**. The European Physical Journal B., 79:121–137, Jan 2011.

[29] KASHIHARA, T.; MICHISHITA, Y. ; PETERS, R.. **Quantum metric on the brillouin zone in correlated electron systems and its relation to topology for chern insulators**. Phys. Rev. B, 107:125116, Mar 2023.

[30] FOX, M.. **Optical Properties of Solids**. Oxford University Press, Oxford, 2010.

[31] DE SOUSA, M. S. M.; CHEN, W.. **Opacity of graphene independent of light frequency and polarization due to the topological charge of the dirac points**. Phys. Rev. B, 108:165201, Oct 2023.

[32] R. R. NAIR, P. BLAKE, A. N. G. K. S. N. T. J. B. T. S. N. M. R. P.; GEIM, A. K.. **Fine structure constant defines visual transparency of graphene**. Science, 320:1308, Oct 2008.

[33] RYU, S.; SCHNYDER, A. P.; FURUSAKI, A. ; LUDWIG, A. W. W.. **Topological insulators and superconductors: tenfold way and dimensional hierarchy**. New Journal of Physics, 12(6):065010, jun 2010.

[34] VON GERSDORFF, G.; PANAHIYAN, S. ; CHEN, W.. **Unification of topological invariants in dirac models**. Phys. Rev. B, 103:245146, Jun 2021.

[35] CHEN, W.. **Optical absorption measurement of spin berry curvature and spin chern marker**. Journal of Physics: Condensed Matter, 35(15):155601, feb 2023.

[36] KANE, C. L.; MELE, E. J.. **Z_2 topological order and the quantum spin hall effect**. Phys. Rev. Lett., 95:146802, Sep 2005.

[37] KANE, C. L.; MELE, E. J.. **Quantum spin hall effect in graphene**. Phys. Rev. Lett., 95:226801, Nov 2005.

[38] CAO, Y., F. V. F. S. E. A.. **Unconventional superconductivity in magic-angle graphene superlattices**. Nature, 556:43–50, Mar 2018.

[39] ROSSI, E.. **Quantum metric and correlated states in two-dimensional systems**. Current Opinion in Solid State and Materials Science, 25(5):100952, 2021.

[40] XIE, F.; SONG, Z.; LIAN, B. ; BERNEVIG, B. A.. **Topology-bounded superfluid weight in twisted bilayer graphene**. Phys. Rev. Lett., 124:167002, Apr 2020.

[41] NAIR, R. R.; REN, W.; JALIL, R.; RIAZ, I.; KRAVETS, V. G.; BRITNELL, L.; BLAKE, P.; SCHEDIN, F.; MAYOROV, A. S.; YUAN, S.; KATSNELSON, M. I.; CHENG, H.-M.; STRUPINSKI, W.; BULUSHEVA, L. G.; OKOTRUB, A. V.; GRIGORIEVA, I. V.; GRIGORENKO, A. N.; NOVOSELOV, K. S. ; GEIM, A. K.. **Fluorographene: A two-dimensional counterpart of teflon**. Small, 6(24):2877–2884, 2010.

[42] LI, Y.; CHERNIKOV, A.; ZHANG, X.; RIGOSI, A.; HILL, H. M.; VAN DER ZANDE, A. M.; CHENET, D. A.; SHIH, E.-M.; HONE, J. ; HEINZ, T. F.. **Measurement of the optical dielectric function of monolayer transition-metal dichalcogenides: MoS_2, $MoSe_2$, WS_2, and WSe_2**. Phys. Rev. B, 90:205422, Nov 2014.

[43] LIU, G.-B.; SHAN, W.-Y.; YAO, Y.; YAO, W. ; XIAO, D.. **Three-band tight-binding model for monolayers of group-vib transition metal dichalcogenides**. Phys. Rev. B, 88:085433, Aug 2013.

[44] LI, H.; QIN, M.; WANG, L.; ZHAI, X.; REN, R. ; HU, J.. **Total absorption of light in monolayer transition-metal dichalcogenides by critical coupling**. Opt. Express, 25(25):31612–31621, Dec 2017.

[45] STAND, N.; MENDOZA, C. D. ; FREIRE, F. L.. **Synthesis of WS_2 by chemical vapor deposition: Role of the alumina crucible**. Crystals, 12(6), 2022.

[46] BIANCO, R.; RESTA, R.. **Mapping topological order in coordinate space**. Phys. Rev. B, 84:241106, Dec 2011.

[47] NAM, N. N. T.; KOSHINO, M.. **Lattice relaxation and energy band modulation in twisted bilayer graphene**. Phys. Rev. B, 96:075311, Aug 2017.

[48] BISTRITZER, R.; MACDONALD, A. H.. **Moiré bands in twisted double-layer graphene**. Proceedings of the National Academy of Science, 108(30):12233–12237, July 2011.

[49] KITAEV, A.. **Anyons in an exactly solved model and beyond**. Annals of Physics, 321(1):2–111, Jan. 2006.

[50] CÁRDENAS-CASTILLO, L. F.; ZHANG, S.; FREIRE, F. L.; KOCHAN, D. ; CHEN, W.. **Detecting the spread of valence-band wannier functions by optical sum rules**. Phys. Rev. B, 110:075203, Aug 2024.

[51] CÁRDENAS-CASTILLO, L. F.; ZHANG, S.; FREIRE, F. L. ; CHEN, W.. **Absorbance marker: Detection of quantum geometry and spread of wannier function in disordered two-dimensional semiconductors**. Phys. Rev. B, 112:085402, Aug 2025.